Quantifying Lung Water Density with Ultrashort Echo Time Yarn-Ball MRI

by

William Quinn Meadus

A thesis submitted in partial fulfillment of the requirements for the degree of

Master of Science

Department of Biomedical Engineering

University of Alberta

Abstract

Pulmonary edema (PE) involves an excess of extravascular lung water (EVLW) due to an imbalance in fluid filtration which results in hypoxia and respiratory distress. Cardiogenic pulmonary edema is a primary clinical feature and therapeutic target in acute heart failure. Current methods in measuring EVLW are lacking, so this study aimed to provide quantitative imaging of water density in the lung parenchyma through MRI.

This thesis illustrates a novel Yarn-Ball (YB) ultrashort TE (UTE) k-space trajectory along side an automated image processing approach. Efficiency-optimized UTE-YB k-space trajectories were designed for breath-hold and free-breathing acquisitions. These provide full torso spatial coverage with minimal T1 and T2* weighting at 3T. A composite of all solid tissues surrounding the lungs (muscle, liver, heart, blood-pool) was used for the lung water density signal referencing and B1-inhomogeneity correction which results in relative water density based images. Automated region-growing based lung segmentation isolates relevant lung parenchyma voxels for final relative lung water density (rLWD) values. Acquisition-time matched 3D radial acquisitions were compared to YB. Sponge phantom experiments were used to validate absolute water density quantification.

Phantom experiments showed excellent agreement between sponge wet weight and imaging-derived water density. Breath-hold (13 seconds) and free-breathing ($\sim$2 minutes) YB acquisitions in volunteers (2.5 mm isotropic resolution) had negligible artifacts and good lung parenchyma SNR (>10:1). Whole lung average rLWD values were 28.6$\pm$3% (automated analysis) with good test/re-test reproducibility (ICC=0.87-0.99). Radial acquisitions with matched durations had significantly reduced fully sampled fields of view resulting in prominent undersampling artifacts.

Quantitative lung water density imaging with an optimized YB acquisition is possible in breath-hold or short free-breathing studies and may prove invaluable in the measurement and tracking of PE.

Preface

This thesis is an original work by William Quinn Meadus. The research project, of which this thesis is a part, received research ethics approval from the University of Alberta Research Ethics Board, Project Name "Development of Magnetic Resonance Imaging", No. 00001460.

Acknowledgements

First, I would like to thank Dr. Richard Thompson for his guidance as my supervisor. This thesis would not have been possible without his encouragement and knowledge. I would also like to thank Dr. Rob Stobbe, who developed and provided support on the key Yarn-Ball k-space acquisition MRI method. I extend my appreciation to my supervisory committee, which includes Dr. Thompson, Dr. Stobbe and Dr. Alan Wilman, for their insightful feedback and advice.

Finally, I would like to express my gratitude for all sources of financial support. This was provided by the Natural Sciences and Engineering Research Council of Canada, the Canadian Institutes of Health Research, the Department of Biomedical Engineering and the University of Alberta. Additional travel funding was provided by the Faculty of Graduate Studies and Research and the Graduate Students' Association at the University of Alberta.

Contents

List of Tables

List of Figures

List of Abbreviations

ARDS	acute respiratory distress syndrome
au	arbitrary units
BH	breath hold
CT	computed tomography
EVLW	extravascular lung water
FB	free breathing
FOV	field of view
HF	heart failure
MRI	magnetic resonance imaging
PE	pulmonary edema
RF	radio frequency
rLWD	relative lung water density
SNR	signal to noise ratio
TE	echo time
TPTD	transpulmonary thermodilution
TR	repetition time
UTE	ultrashort echo time
YB	yarn-ball acquisition

Chapter 1

Introduction

1.1 Pulmonary Edema

1.1.1 Lung Anatomy

The lungs contain a complex system of air channels and compartments to enable gas exchange. Air enters the lungs through the trachea then splits into the two bronchi, branches further into the bronchioles and terminates at the alveoli. The network of alveoli forms the sponge like lung parenchyma and maximizes available surface area for gas exchange. An average 30 year old male has 130 m^2 of alveolar surface area [1]. Wrapping around individual alveolus are a set of pulmonary capillaries, each of which has a thick and thin edge (a cross section is displayed in Fig. 1.1). The thin edge allows for gas exchange through the air-blood barrier, while the thicker edge contains an interstitial space in which liquid and solute exchange occurs from the capillary lumen [1]. This interstitial space of the interalveolar septum is directly connected to the interstitial tissue surrounding arterioles, venules, and bronchioles, where the terminal branches of the pulmonary lympatics are located, forming a continuous path to the lymphatic system [2].

Fluid filtration between the capillaries and interalveolar interstitial space

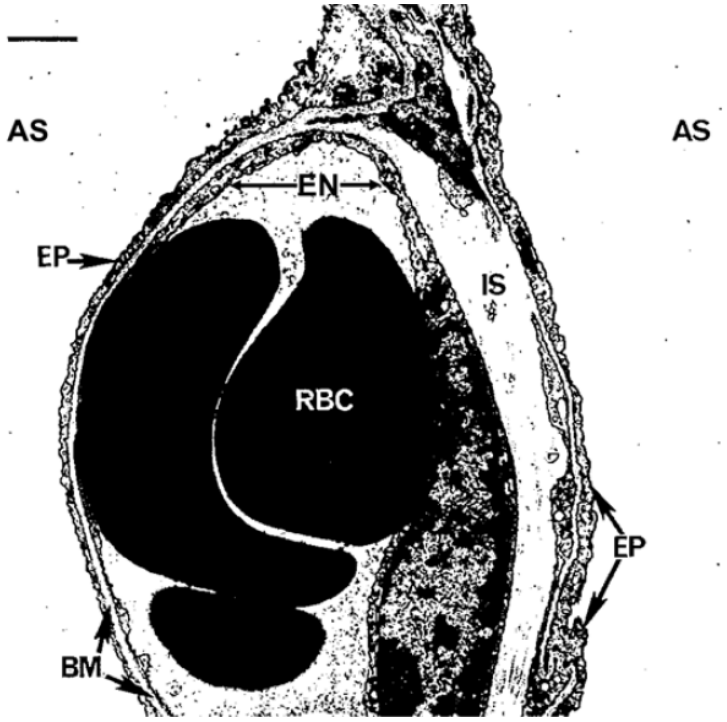

Figure 1.1: Electron micrograph showing the cross-section of a pulmonary capillary. Labels represent the alveoar space (AS), interstitial space (IS), epithelium (EP), endothelium (EN), basement membrane (BM) and red blood cell (RBC). Figure from Murray [1].

is governed by the starling equation [3]:

$$J_v/A = L_p([P_c - P_i]) - \sigma[\pi_p - \pi_i] \tag{1.1}$$

where J_v is the rate of filtration, A is the endothelial surface area L_p is the hydraulic conductivity of the membrane, P_c and P_i are the capillary and interstitial hydrostatic pressures respectively, σ is the reflection coefficient, and finally π_p and π_i are the plasma protein and subglycocalyx oncotic pressures respectively. Fluid is constantly filtering from the capillaries into the interalveolar interstitial space at a rate described by equation 1.1. Physical exertion causes filtration to increase greatly, but the lymphatics swell to compensate. Filtrate exits the lungs by flowing towards the hila (lung roots - a complex collection of bronchi, arteries and veins) if nearer the center of the body, or towards the pleura (sac surrounding the lungs) if near the outside edge of the lung [4]. All together, fluid is constantly leaking from the pulmonary capillaries into interstitial spaces but then reabsorbed into the bloodstream via the lymphatics.

1.1.2 Disease Characteristics

Pulmonary edema (PE) is the result of fluid filtration exceeding a threshold capacity of lymphatic drainage, leading to increased extravascular lung water (EVLW). Generally, the intersitial spaces fill first and in severe cases the aleveolar spaces follow. Normal lung function and gas exchange are impeded, hence people suffering from PE will have symptoms of hypoxia and respiratory distress. Instances of PE are traditionally categorized into two types, cardiogenic and non-cardiogenic [2]. In the case of cardiogenic PE, the hydrostatic capillary pressure (P_c) increases greatly from left sided heart-failure (HF). Non-cardiogenic PE occurs when endothelial permeability (equivalent to hydraulic conductivity L_p) increases, which allows water and protein to leak into the in-

teralveolar interstitial space. Acute respiratory distress syndrom (ARDS) is a prominent example of non-cardiogenic PE. Further subdivisions of PE origins have been proposed by Ketai et al. who also consider the state of the alveolar epithelium [5]. It may be damaged by "stress-failure" due to extreme pressure or the presence of diffuse alveolar damage as found in ARDS. PE limited to the interstitial spaces causes less distress and clears more quickly, while fluid leaking through the alveolar epithelium and filling the alveoli is difficult to clear and leads to severe symptoms.

In general, outcomes are poor. Mortality is 12% in-hospital and 40% after one year for patients hospitalized with acute PE [6]. Cardiogenic PE is a major symptom of HF, which appears in at least 50% of heart failure patients [7]. In fact, acute HF patients are often hospitalized because of congestion due to PE as opposed to reduced cardiac output [8]. Cardiogenic PE cases are common considering heart failure prevalence is 23 million worldwide [9], these cases provide the main motivation for this study. ARDS is a less common but severe manifestation of PE. It has many potential sources including pneumonia, sepsis, and pancreatitis. ARDS patients comprise 10.4% of ICU admissions and leads to a 40% mortality rate [10].

1.1.3 Current Measurement Methods

Accurate measurement of EVLW in vivo is challenging and not routinely performed. In vitro, EVLW measurement is straight forward through gravimetry, which involves the comparison of dry and wet weights of an excised lung. It is often used to validate animal studies and serves as a gold standard when available [11].

The most readily available tool to diagnose PE in vivo is the stethoscope. The presence of "fine crackles" during auscultation indicates the presence of insterstial edema. While useful, auscultation has no way to distinguish mild from severe PE and suffers from interobserver variability [12].

In clinical practice, chest X-ray is often used to diagnose PE due to its wide availability and rapid examination of the lungs. However, diagnosis of PE relies on user-recognition of specific image features (example in Fig. 1.2), also suffers from high interobserver variability, and lacks quantitative ability [12]. Computed tomography (CT) provides a high resolution picture of the lungs and is the gold standard for the diagnosis of numerous lung diseases, including PE [13](Fig. 1.3). However, the required large dose of ionizing radiation is clear downside, especially when tracking disease progress through repeated measurements. Also, CT (X-rays) does not distinguish the presence of increased solid tissues, such as fibrosis, and increased water.

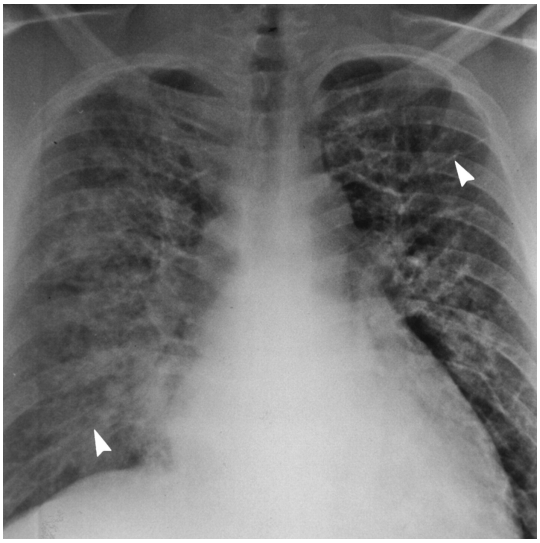

Figure 1.2: A case of cardiogenic PE in a 33-year-old man observed by chest x-ray. The arrowheads point out key "bilateral Kerley line" features in PE diagnosis. Figure from Gluecker et al. [14].

A newer technique, lung ultrasound, provides a safe and non-invasive bedside method to assess PE, based on counting characteristic comets or streaks on the images associated with edema (Fig. 1.4). However, the technique is still in devlopement without any large-scale randomized trials and is limited by the "semi-quantitative" nature of counting image streaks as a measure of water density [16].

Finally, transpulmonary thermodilution (TPTD) is the most established

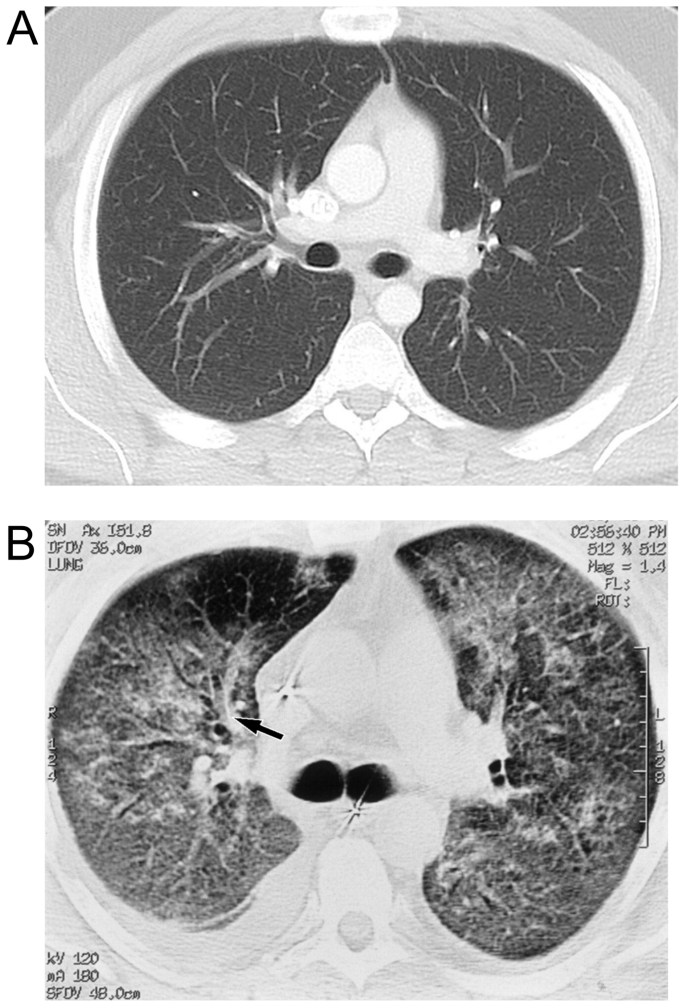

Figure 1.3: **(A)** A normal CT of the chest in a healthy adult (Case courtesy of Dr Andrew Dixon, Radiopaedia.org, rID: 36676 [15]. **(B)** A CT of the chest in a 53-year-old man with cardiogenic PE (figure from Gluecker et al. [14]).

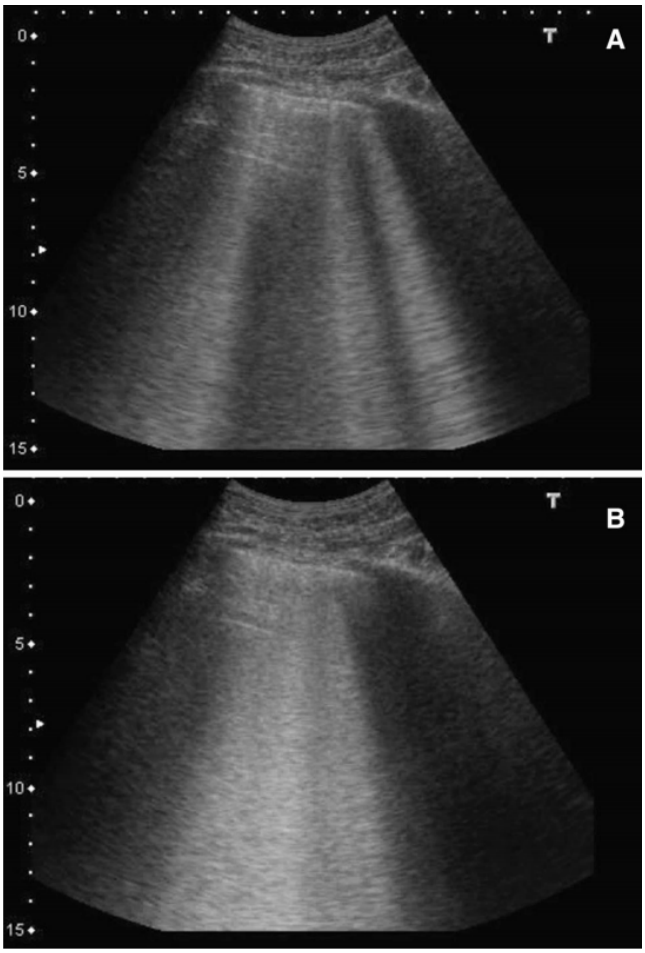

Figure 1.4: The appearance of cardiogenic pulmonary edema in lung ultrasound. A region with moderate edema **(A)** and substantial edema **(B)**. Figure from Cortellaro et al. [17].

method in providing quantitative PE evaluation, specifically the targeted EVLW volume [18]. It has also been verified with gravimetric examinations [19]. Despite the accuracy of the technique, catheter insertion is required and EVLW volume can only apply to the entire lungs, with no sensitivity to regional variations in water density.

1.2 Study Motivation

Pulmonary edema is a common condition with many potential causes and is often a sign of underlying health problems. Despite its clinical significance, accurate quantification and tracking of the condition is lacking. An array of measurement methods exists, but each has significant drawbacks, as summarized in the previous section. This study introduces a new MRI based method to track the disease. Our goal is to use the inherent advantages of MRI, being non-invasive, having no ionizing radiation and intrinsically measuring water content. We apply the novel Yarn-Ball (YB) k-space acquisition scheme, which allows for ultrashort TE (UTE), full-sampling of k-space, high SNR, and motion correction in a patient-friendly total scan duration. On top of this, new methods for signal referencing (to provide quantitative water density), background field correction, and lung masking techniques were developed to analyze the images. All together, we aimed to provide a complete lung water quantification package with clinical viability.

1.3 Magnetic Resonance Imaging Methods

1.3.1 Lung MR Basics

Magnetic Resonance Imaging (MRI) directly measures water content and can provide full 3D images of the lungs without being invasive or requiring ionizing radiation. However, the lungs present unique challenges to MRI.

First, the sparse structure of lung parenchyma leads to low proton density and correspondingly low signal yield. Because of this, signal to noise ratio (SNR) will always be relatively low when compared to the majority of other tissues, regardless of MRI protocol.

Second, cardiac and respiratory motion must be accounted for. The natural expansion and contraction of the lungs over breathing cycles of 2-4 seconds can cause signal to be acquired at varying respiratory phases, leading to significant blurring in the final image. Motion of the heart and pulsatility of the blood can similarly give rise to image artifacts, depending on the acquisition method. Limiting the total acquisition time to a single breath hold is the most straight forward solution but greatly limits sequence parameters. Gating techniques allow for free breathing acquisitions but add complexity and lengthen scan times (section 1.3.6).

Third, the many air-tissue interfaces in lung parenchyma lead to extremely fast transverse relaxation (short T2*) and potentially large signal losses. Magnetic susceptibility differences between air (0.36×10^{-6}) and tissue (-11.0×10^{-6} to -7.0×10^{-6}) [20] add magnetic field inhomogeneity, which de-phases the transverse magnetization. Lung T2* is 2.11($\pm$0.27) ms at 1.5T and 0.74($\pm$0.1) ms at 3.0T [21]; these values are well below the values of the more commonly imaged tissues, with T2* values of several tens of milliseconds.

1.3.2 MRI Methods

A wide variety of MRI pulse sequences have been used to image the lungs, including spoiled gradient echo, balanced steady state free precession, spin-echo, and ultra-short echo time (UTE) approaches. While spin-echo acquisitions (which are T2 weighted) largely eliminate the signal loss from T2* effects, they remain sensitive to T2 ($\sim$ 40ms in the lungs at 1.5 T [22]) and are relatively slow and sensitive to motion(cardiac and respiratory). With quantification of EVLW as the goal, the sequences which can provide proton density weighting

and minimal motion artifacts are desired. In particular, pulmonary edema has been shown to increase T1 and T2 in lung parenchyma [23] and this lack of knowledge of the T1 and T2 values further highlights the need for minimal signal weighting.

The spoiled gradient echo (SPGR) sequence is efficient for imaging the entire lung volume (i.e. 3D SPGR is relatively fast) but generally results in low SNR with the required short repitition times (TR). Transverse signal decay from excitation to signal acquisition is described by:

$$M_{xy}(TE) = M_{xy}(0)e^{-TE/T2^*} \tag{1.2}$$

$M_{xy}(0)$ is the maximum available transverse magnetization, which is a function of the pulse sequence parameters. In order to avoid unwanted signal loss when using gradient-echo acquisitions, one must ensure TE $\ll$ T2*. Also, the relatively long lung T1 (1397$\pm$214 ms at 3.0 T [24]) can lead to significant T1-weighting with the short TR values desired for fast imaging. In addition, the T1 values of other tissues near the lungs may also need to be accounted for, including the liver (812$\pm$64 ms), skeletal muscle (1412$\pm$13 ms), blood (1932$\pm$85 ms) [25], myocardium ($\sim$1160 ms) [26], and fat ($\sim$400 ms) [27]. Signal intensity in a partial saturation based acquisition, which includes T1 weighting depending on the applied flip angle, is described by equation 1.3 [28].

$$S = \frac{S_0 sin(\alpha)(1 - e^{-TR/T1})e^{-TE/T2}}{1 - e^{-TR/T1}cos(\alpha)} \tag{1.3}$$

Careful consideration of TR values, T1 values and flip angles are necessary with this approach of lung water imaging.

Lastly, unwanted signal loss from the short lung T2* values is limited by the use of ultrashort echo time (UTE) methods, which typically use center out k-space acquisitions (section 1.3.4) to achieve sub-millisecond TEs. For comparison, applying equation 1.2 to the lung T2* of 0.74 ms (3T) results in

approximate signal yields of 25% at TE = 1 ms and 87% at TE = 0.1 ms. While UTE approaches (which can offer TE $\ll$ T2*) do address the T2* signal losses, there are several challenges that must be overcome for their practical application, which is detailed in section 1.3.4 below.

1.3.3 Quantifying Lung Water

Considering the proportional relation between water, spin density and MR signal, measuring EVLW with MRI appears to be the optimal imaging modality. However, MRI signal is typically expressed in arbitrary units (au), given the many factors that affect the intensity of the acquired signal. Direct absolute signal quantification usually isn't practical due to radio-frequency (B_1) transmit and receive inhomogeneities, the requirement for a signal reference, unwanted T1, T2 or T2* weighting and other factors such as off-resonance dependence.

Multiple early MR studies attempted to quantify lung water with animal studies. Such studies employed excised lungs from an array of animals, including rats [29](Fig. 1.5), dogs [30](Fig. 1.6), and pigs [31]. They used external, pure water phantoms as reference signal. These studies succeeded in correlating lung SNR/proton density with gravimetric results, but were impractical with long scans and generally poor image quality. The applied MRI pulse sequences all led to significant image weighting, either being T2* weighted with SPGR sequences and TEs of several milliseconds, or T1 and T2 weighted when spin echoes were applied. A more modern study, which used excised pig lungs, showed a strong correlation between MRI derived lung water and gravimetric results using a gradient echo sequence [32]. This study attained 8s acquisition times with TE values of 1.03 ms and 1.40 ms, but this still leads to significant signal decay in lung parenchyma. In addition, T1 was not taken into consideration for this study, which would be of concern with a TR of 10 ms and 10° flip angle.

As described earlier, UTE methods limit T2* decay and have potential for

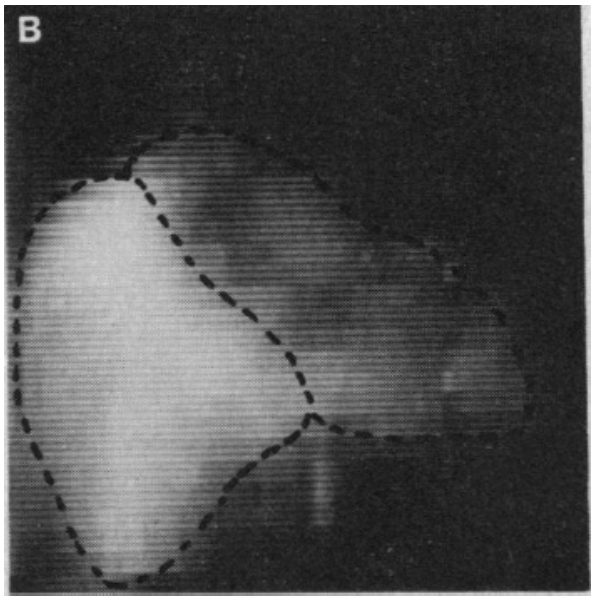

Figure 1.5: NMR image of isolated rat lungs obtained with a line-scan technique for quantitation of lung water in 1982. Figure from Hayes et al [29].

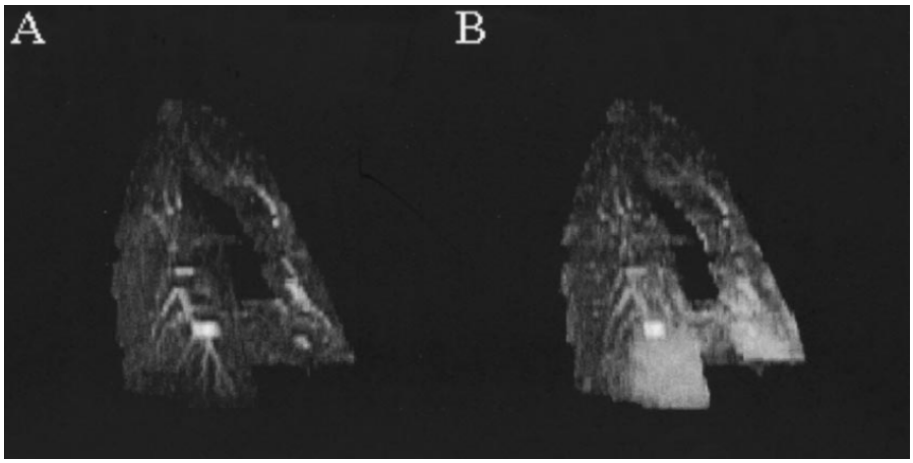

Figure 1.6: MRI of dogs lungs **(A)** before and **(B)** after injury to induce pulmonary edema. Figure from Caruthers et al [30].

more accurate lung parenchyma signal measurement. Molinari et al. demonstrated the advantage of quantifying water content with UTE over a gradient echo sequence in a "sponge phantom", which mimics the lung parenchyma [33].

These studies presented the ability to quantify lung water in ideal scenarios, but many more challenges are present in vivo. First, the effects of cardiac and respiratory motion must be considered and the influence of the degree of lung inflation should be accounted for. With lung inflation varying by several litres in adults, water density will also vary greatly at different stages of the respiratory cycle. T2* has also been found to be affected by inflation, which adds uncertainty in T2* weighting [34]. Second, pure water reference phantoms are impractical due to large B_1 field excite and receive inhomogeneities. For example, when using a chest coil, signal in the chest muscle lies much closer to the receive array and returns much higher signal; therefore, water phantoms placed outside the body would also return inflated values, experiencing very different B_1 fields than the lungs. Finally, when not excised and isolated, defining the lung parenchyma regions is more difficult. A "mask" is required to describe where the lung parenchyma lies, while excluding major vasculature, skeletal muscle, and the liver (section 1.4.3). Better definition of lung vasculature to improve the masking process is an important benefit of higher resolution images.

Similar to measuring lung water, some studies have examined "lung density", being analagous to CT. These have used muscle tissue to calibrate lung signal. Lederlin and Crémillieux used stack-of-stars UTE MRI to examine lung density [35]. They drew ROIs in lung parenchyma and muscle regions close in proximity to compare signals (Fig. 1.7), assuming each area experienced similar MRI pulse sequences (e.g. B_1 values). They found 34% and 58% water content (relative to muscle) in gravitationally non-dependent and dependent regions respectively. Several studies examined the density of neonatal lungs, which suffer less from B_1 inhomogeneity and motion artifacts due to their small

size. In a gradient echo study, Walkup et al. used mean chest soft tissue signal to normalize entire lung areas [36]. Here two different lung masks were defined with empirically chosen thresholds. A 45% signal cut off (relative to mean chest soft tissue signal signal, Fig. 1.8) was used to define high signal areas (potential edema, fibrosis etc.) and another with 4% signal to define low signal (alveolar simplification). 3D radial UTE MRI was used in the Hahn [37] and Higano [38] in neonate studies, which also used mean muscle tissue signal but differing masking methods. Hahn segment each lung into 3 compartments, upper lower and middle, to provide 6 regions between the two lungs. Higano used a manually guided region growing algorithm to mask each lung and avoid major pulmonary vessels.

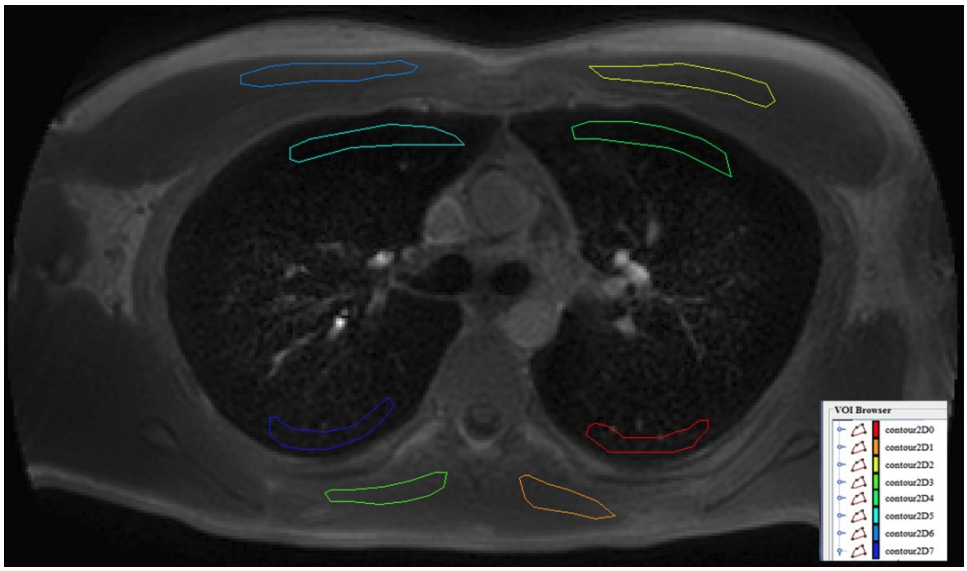

Figure 1.7: Healthy control lung MRI. ROIs drawn to determine lung density based on muscle signal yield. Figure from Lederlin and Crémillieux [35].

Each of the above methods for quantifying lung signal have limitations. Any user input, which could be an arbitrary threshold or manually drawn ROI, add inter observer variability. B_1 field effects must still be considered, as muscle tissue from different parts of the body will provide varying signal yield depending on MRI set up (coil location, body position etc.). Last, assumptions on either muscle water content or density were made to report quantitative

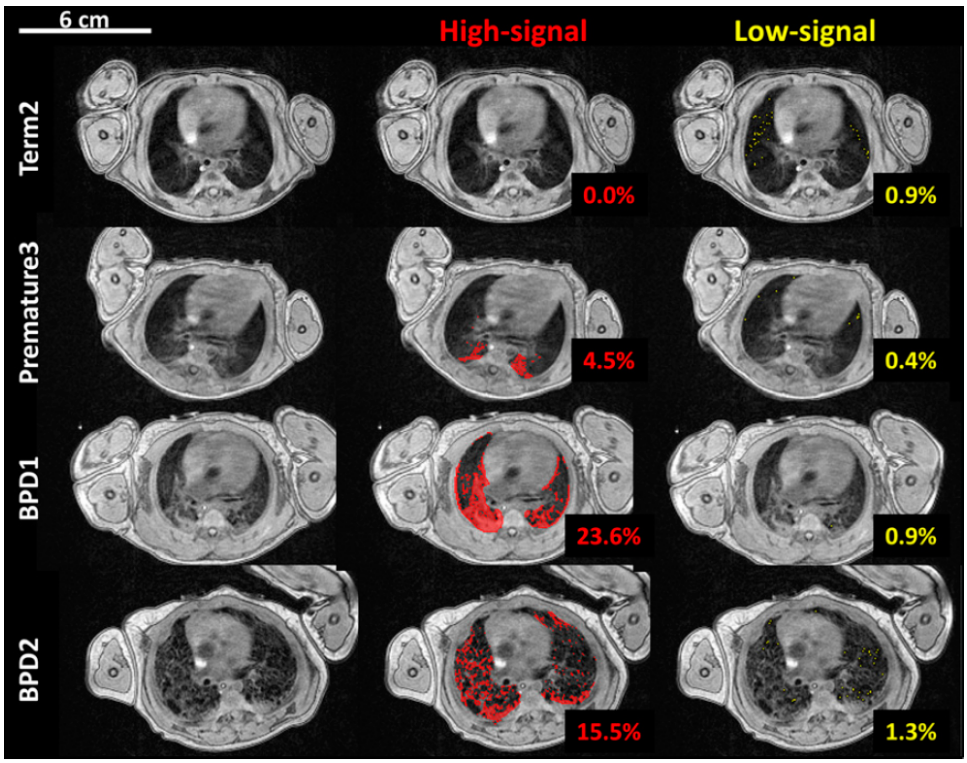

Figure 1.8: MRI of parenchyma density in neonates. Includes a full-term control subject (Term 2), a premature patient (Premature3) and two bronchopulmonary dysplasia patients (BPD1 and BPD2) . Figure from Walkup et al. [36].

results. The accuracy and consistency of muscle composition between different people is undetermined and a potential source of error.

1.3.4 UTE K-space Acquisition

In order achieve ultra short echo times (UTE), k-space acquisition must begin immediately after excitation (i.e. to put the the center of k-space within $\sim$100μs of excitation or less). This sampling approach is not compatible with Cartesian trajectories, which require pre-phasing gradients (i.e. requiring time) to start k-space readouts at the edges of k-space and the subsequent sampling of k-space from the edge to the center. The most commonly used 2D UTE method is radial sampling of k-space, which acquires arms in a center out fashion and looks like a "star" when complete (Fig. 1.9A). Full sampling (fulfilling the Nyquist criterion) is determined by the distance between k-space samples at the edge of k-space, where the distance between the radial arms is largest. This is determined from the desired image parameters, where resolution relates to k-space maximum ($RES = 1/(2k_{max})$) and field of view (FOV) relates to distance between k-space samples ($\Delta k = 1/FOV$). Therefore, sampled data covers a circle of radius k_{max} and points on this surface must be separated by Δk. The number of k-space points per readout (if spaced equally on a line) R is then:

$$R = k_{max}/\Delta k = FOV/(2 * RES) \tag{1.4}$$

Equation 1.5 determines the necessary number of trajectories (or arms) for the Nyquist criterion to be reached, which is generally a much larger number than with Cartesian acquisition.

$$N_{traj} = 2\pi R \tag{1.5}$$

Another commonly used 2D UTE method, spiral imaging [39], also begins center out to enable UTE, but requires less trajectories to fill k-space at the

cost of longer readout times and potential image blurring. Both 2D radial and 2D spiral imaging methods can be adapted to 3D with slab excitation and slice encoding, being called stack-of-stars and stack-of-spirals respectively, however the required slice-oriented phase-encoding gradients will increase the minimum echo.

To obtain isotropic 3D resolutions and avoid slice encoding altogether, 3D k-space acquisitions can be applied. 3D radial is the standard version of this, sometimes being called "koosh-ball" (Fig. 1.9B). This however, is even less efficient than 2D radial, and follows equation 1.6 [40].

$$N_{traj} = 4\pi R^2 \tag{1.6}$$

For full Nyquist sampling, A 3D image with an FOV of 300 mm and 2.5 mm ($R = 60$) isotropic resolution requires 14,400 trajectories with Cartesian k-space sampling, while requiring 45,238 with 3D radial filling.

Another 3D UTE k-space sampling method is the 3D cones trajectory [41]. First, the number of cone surfaces is determined to adequately cover a sphere of k-space as in Figure 1.9C. Then the number of trajectories per cone is determined based on the necessary interleaved spirals. Calculation of total trajectories and efficiency depends on desired imaging parameters, but a significant reduction of trajectories is seen when readout times exceed 2.0 ms. Finally, FLORET [42] is a 3D spiral UTE sequence designed specifically for the short T2* of the lungs.

Modified slice selections must be applied to minimize or eliminate the need for slice select refocusing lobes. These include "split sinc" pulses for 2D images, non-selective hard pulse sequences for 3D imaging and selective RF pulses with slab-select gradients. An overview of these is given by Quian Y and Boada FE [45].

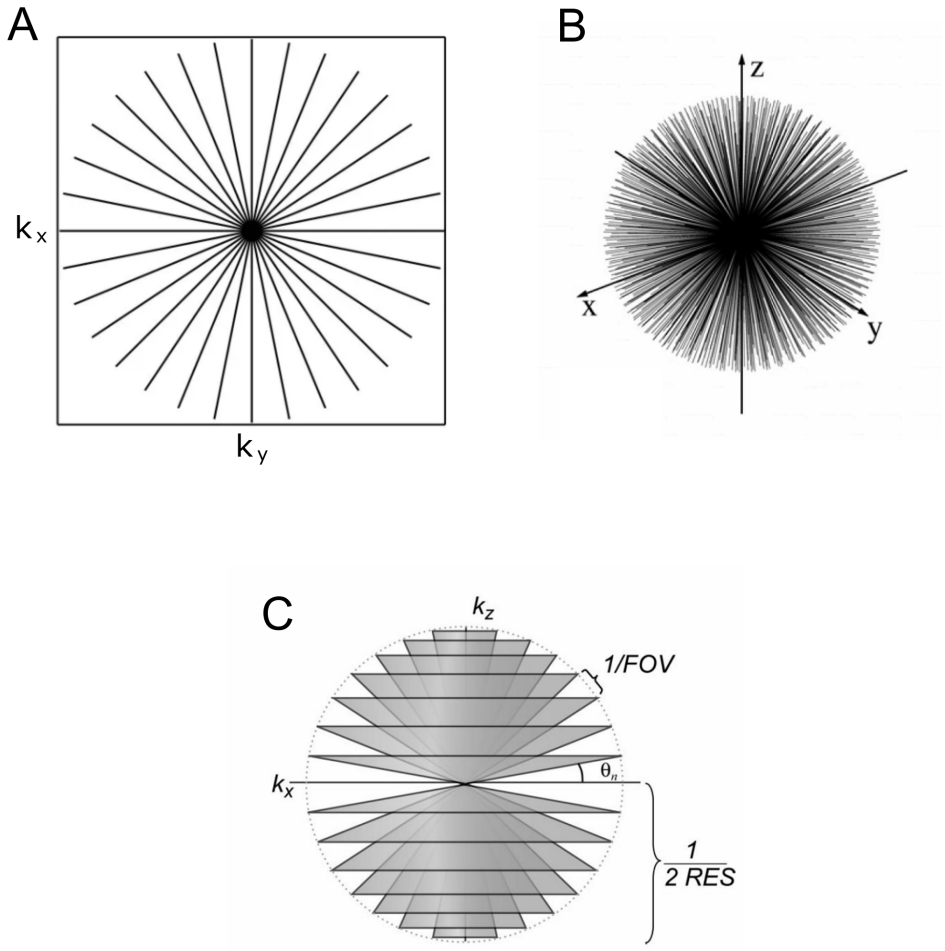

Figure 1.9: **A)** 2D radial k-space sampling figure modified from Ferreira PF et al. [43]. **B)** 3D radial k-space sampling figure from Herrmann KH et al. [44]. **C)** Layout of cone surfaces in the 3D cones trajectory (figure from Gurney PT et al. [41]).

1.3.5 Yarn-Ball k-space Sampling

An alternate 3D UTE sampling approach, called Yarn-Ball (YB) [46] was designed to sample k-space along non-linear paths that are optimized for acquisition efficiency. Also beginning center out, a straight radial path is followed until a threshold distance is reached. This threshold is equal to $\rho * R$, where ρ is the "radial fraction" (between 0 and 1). Past this threshold, the trajectory begins to "wind" around the center, analogous to winding a ball of yarn. The winding phase is governed by the following equations:

$$\dot{r} = \rho^2 / r^2 \tag{1.7}$$

$$\dot{\theta} = \pi R \dot{r} \tag{1.8}$$

$$\dot{\phi} = 2\pi R r \dot{\theta} \tag{1.9}$$

Here, r is the "relative radial distance" (normalized to R), θ is the polar angle, and ϕ is the azimuthal angle. Essentially, for every radial k-space step, the trajectory must sweep from 0 to π radians in the polar angle. Then for each step in the polar angle, the azimuthal angle must rotate through 2π radians enough times for full sampling at that radius. This "winding" is segmented into "discs" and "spokes". There are N_{spokes} for each of the N_{discs} and $N_{spokes} * N_{discs} = N_{traj}$. This results in the following equations:

$$\dot{\theta} = \pi R \dot{r} / N_{discs} \tag{1.10}$$

$$\dot{\phi} = 2\pi R r \dot{\theta} / N_{spokes} \tag{1.11}$$

The most efficient and evenly spaced sampling occurs when $2N_{discs} =$

N_{spokes}. With radial like acquisition occurring within $\rho * R$, equation 1.5 holds when the discs or spokes are considered on a 2D plane. This means the value of ρ is constrained by the number of trajectories:

$$\rho = min(N_{discs}/\pi R, N_{spokes}/2\pi R) \tag{1.12}$$

That is, $\rho * R$ is equivalent to the maximum radius where Nyquist sampling can be achieved with normal radial trajectories. Everything beyond that radius is filled with yarn ball winding. An example trajectory is displayed in Figure 1.10.

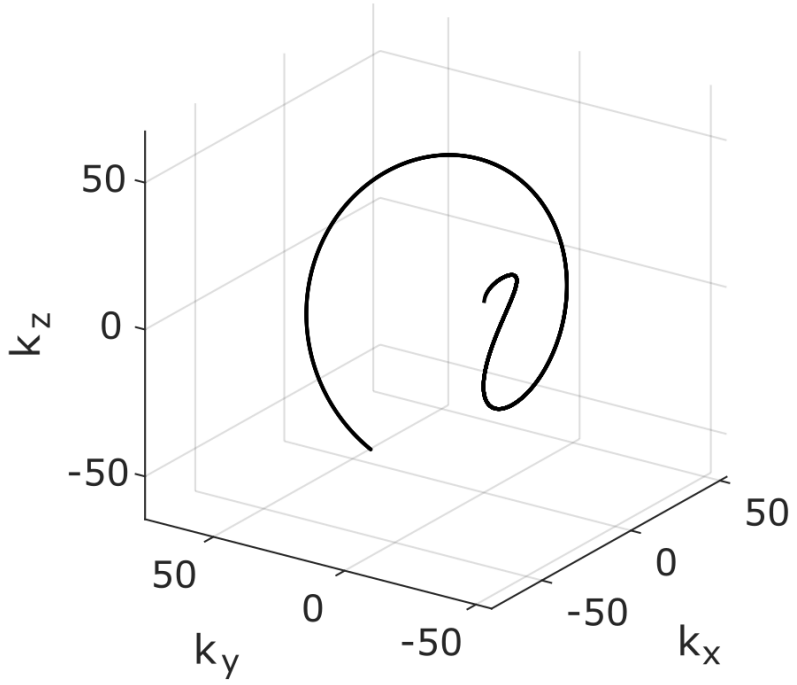

Figure 1.10: An example trajectory displaying the center out and winding nature of Yarn-Ball acquisition.

The speed and coverage of the winding portion of each trajectory is limited by a few key aspects including gradient strength, nerve stimulation and readout duration. As compared to the pure radial trajectories, YB trajectories benefit greatly from longer readouts, being able to "wind" further in a single trajectory

and cover k-space with few trajectories, reducing scan time. However, depending on factors such as T2* times and off-resonance frequencies, this can lead to significant blurring and more complex image artifacts.

In conclusion, based on a selected resolution, FOV, and readout duration, optimal scan time is achieved by minimizing the number of trajectories (constrained by hardware (gradient slew rates) and nerve stimulation). Yarn ball trajectories generally cannot be implemented based on the above equations alone, so trajectories are "stretched" near the center and "contracted" near the peripheries to avoid excessive gradient switching. In comparison to the 45,238 trajectories necessary for 3D radial in the previous example, yarn ball required only 6,555 trajectories to achieve the same image parameters (detailed in Chapter 2).

In addition, both radial and YB methods can be used in a "dual echo" fashion to obtain a second image immediately after the first with a longer TE. In the case of radial, the gradients simply reverse to trace back along the same path to the center of k-space. In yarn ball, the trajectory continues in the direction it finished after the first echo and winds back into the center. These dual echo image sets can be useful for generating T2* contrast, for either T2* estimation (which may be increased in the presence of edema) or to generate black-lung images (to enhance lung parenchyma segmentation). Dual echo radial acquisition has been applied to map T1 and T2* in the lungs [47].

Finally, YB can also be implemented in a "golden ratio" fashion. YarnBall is generally implemented such that the initial trajectory projections away from the center of k-space are first rotated about a disk and then rotated about subsequently rotated disks. Thus, these initial trajectory projections follow a progressive evolution pattern about a sphere. In the 'golden ratio' approach, trajectories are not 'played-out' sequentially, but are played out over steps of size S, where $S \approx N/\phi_g$. Here, N is equivalent to the total number of trajectories required to fully sample a sphere and ϕ_g is the golden ratio

($\phi_g \approx 1.618$). For example, when $N = 10$, the order is 1,7,3,9,5,2,8,4,10,6 (here S is rounded to 6, except for the step from 5 to 2 where $S = 7$). The value of golden ratio indexed YB is that any data subset will contain an approximately 'uniform collection' (or uniform density) of trajectories from across the full YB set, which is useful for retrospective gating as described in section 1.3.6 below.

1.3.6 Respiratory Motion Correction

Both cardiac and respiratory motion must be accounted for in order to avoid motion blurring. Cardiac motion is not a concern when the center of k-space is sampled repeatedly, as in center out UTE trajectories. What results in such cases is an averaging of the heart motion leading to a blurred or averaged heart image, but no artifacts in surrounding areas. Therefore, Yarn-Ball k-space acquisition is relatively unaffected by cardiac motion.

On the other hand, respiratory motion affects the entire torso and requires special attention. To avoid image blurring or artifacts due to this, the simplest solution is to have patients hold their breath for the duration of the scan. Of course, this severely limits scan time and thus k-space coverage (spatial resolution, signal to noise, etc.). Free breathing acquisitions are feasible when information on respiratory position is available. The respiratory signal, often called a navigator signal, can be used to trigger data acquisition at targeted respiratory phases or positions. A direct way to obtain a navigator signal is through a physical device, such as a thoracic belt to measure torso expansion [48].

Alternatively, navigator echoes use additional RF pulses to determine diaphragm position during the scan [49]. Conventional navigator echoes use a "pencil beam" excitation, which is reconstructed into a single line scan. Aligning multiple line scans side by side will show time-varying motion along the axis of the pencil-beam, providing diaphragm position information over time. Navigator echoes are quite common and useful, but the necessity for additional

RF pulses complicates the sequence.

Self-navigators can be obtained from the k-space data itself if the center is repeatedly sampled throughout a sequence, as is the case with most UTE acquisitions. This source of navigator signal is the most convenient to implement because no modifications to the scanning procedure are necessary (no interruption of continuous data acquisition). The k-space center represents a DC signal which is the total signal from the entire volume obtained without any spatial frequency encoding. This varies slightly with chest and diaphragm position, meaning respiratory information can be extracted from this signal. Coils in different positions will be affected differently by this position, so individual coil locations should be considered when extracting data. A coil resting on the chest will be affected much greater than one close to a shoulder. One way to combine information from multiple coils is through principle component analysis (PCA) [50]. PCA combines variables in such a way to maximizes variation, so coils are combined optimally to highlight respiratory motion. This approach is applied for all free-breathing studies in Chapter 2. However, this method can only provide a relative as opposed to an absolute diaphragm position; physical motion distances are unknown.

Self gating signals can also be derived from low resolution images reconstructed with a "sliding window" approach as described by Tibiletti et al. [50]. From this series of images, the diaphragm position can be tracked in a similar fashion to a pencil beam navigator, without the additional RF pulses.

With a navigator signal in hand, the MRI data needs to be organized in such a way to avoid motion artifacts. "Gating" involves only using MRI data corresponding to a certain respiratory position in making an image. The criteria for gating can be chosen freely, for example, being based on absolute diaphragm position or a percentage of respiratory phase. Generally, narrower criteria results in images with less motion artifacts but a longer acquisition time. Gating can be done "retrospectively" or "prospectively". Retrospective gating

includes continuously acquiring data and "binning" the data in post-processing. Prospective gating involves determining respiratory position in real time and only acquiring data at certain times. This is more complex to implement but has much more efficient data acquisition.

1.3.7 Coil Combination

When imaging the lungs, chest and back coils arrays provide much higher SNR than the full body coil. When a coil array is used, the data from each coil is reconstructed into individual images. From these images we see excellent SNR in a local region near the coil, and low SNR in distant areas of the FOV. Combination of these images is necessary to generate an image which covers the entire FOV adequately. Although easy to implement, simply averaging the images results in noise amplification. A given pixel will receive equal contribution from all coils, regardless of proximity and SNR, which means coils distant from said pixel will mostly contribute noise. Considering this, coil sensitivity profiles are useful since they can weigh the contribution of each coil on a pixel by pixel basis. Coils closest to a given pixel will be weighed highest, while those further (and mostly contributing noise) will be suppressed. Since obtaining full coil sensitivity profiles (B1 receive maps) in-vivo is impractical, we applied the SUPER (summation using profiles estimated from ratios) method described by Bydder et al. [51]. This method involves estimating coil profiles by applying heavy low pass filters to the image it produced. The brightest pixels in a coil image are generally the closest, so this serves as a useful approximation despite disregarding signal variations from the subject itself. The challenges of correction for non-uniform signal intensity when using coil arrays, which is necessary to estimate lung water content, is described below (section 1.4).

1.3.8 SNR Reconstruction

In order to obtain true SNR values on a voxel by voxel basis, the approach described by Kellman and McVeigh was applied [52]. This method involves generating a noise covariance matrix between all coil elements with pure noise data (obtaining signal without any RF gradients or excitation). Noise acquired at a different bandwidth from image data must also be scaled accordingly. All aspects of the reconstruction process (windowing, inverse fourier transform, sampling density compensation) must be normalized to avoid signal biasing. The noise covariance matrix is factored into the final reconstruction during array combining. No magnitude image correction was necessary as B1-weighted combining [51] was also applied.

1.4 Image Processing

1.4.1 Image Normalization and Surface Fitting through Tikhonov Regularization

Surface coil signal reception is optimal for SNR considerations, but results in non-uniform signal intensities over space. Also, the transmit (B_1+) field form the body coil cannot be assumed to be uniform over larger fields of view, resulting in spatially varying flip angles and thus signal yield. An image normalization method was developed to address these challenges, based on the use of all solid tissues surrounding the lungs (reference tissues: muscle, liver, heart, blood pool) as a global signal reference. This approach assumed that all tissues have a similar water density, which is well documented with values ranging from 70% to 80% [53, 54, 55].

The image normalization process applied relied on generating a best-fit surface from the reference tissues only, with large regions of missing data (e.g. from the lungs, bones). Surfaces were generated by a method derived from John

D'Errico's "gridfit" MATLAB function [56]. This allows for the generation of a smoothly varying surface over a sparse image with a high level of control of the properties of the best-fit surface. Each pixel in an image can be thought of as a linear equation of the form:

$$a_n x_n = b_n \tag{1.13}$$

where a_n is an independent variable representing a pixel index (n total pixels, $n = i * j$, i pixels tall and j pixels wide), x_n is a parameter setting the pixel brightness, and b_n is the resulting pixel. Therefore, each individual pixel of the image is represented by a simple linear equation. The set of these equations is best represented in matrix form:

$$Ax = b \tag{1.14}$$

In this form, it can be seen as a multiple linear regression problem where matrix A has m rows and n columns and b is a vector of length m ($m = n$ when all pixels are included). A surface could be generated with ordinary least squares regression, which seeks to minimize the sum of residuals:

$$min_x\{\|Ax - b\|^2\} \tag{1.15}$$

However, in an image with missing pixels, we only have m equations for each available pixel and n columns for the total pixels($m < n$). Hence, the linear algebra problem becomes underdetermined and ill-posed. This means simple linear algebra methods cannot be applied. Tikhonov regularization [57] (aka ridge regression) addresses this problem by adding factors to the equation that bias the solution towards a certain goal (can also be applied to a well-posed problem). The form of the Tikhonov matrix will determine this bias. A second order central difference approximation may be applied within one of these

matrices, and appears as follows:

$$f''(x) \approx \frac{f(x+h) - 2f(x) + f(x-h)}{h^2} \tag{1.16}$$

Which simplifies if h is set to 1 as the index difference between neighbouring pixels. Final pixel value b_n is equivalent to $f(x)$

$$b''_n \approx b_{n+1} - 2b_n + b_{n-1} \tag{1.17}$$

A Tikhonov matrix (L) is formed from a set of these equations, applied in both the i and j directions. For the surface fitting problem with missing data, setting these values to zero will minimize variation in slope and enforce smoothness in the generated surface.

$$Lx = 0 \tag{1.18}$$

Adding these constraints to the least squares problem:

$$min_x\{\|Ax - b\|^2 + \lambda\|Lx\|^2\} \tag{1.19}$$

Generally, the tikhonov matrix is multiplied by a constant known as a regularization parameter (λ). Solving for the minimum of equation 1.19 results in the final equation for the approximated x parameters:

$$x_\lambda = (A^T A + \lambda^2 L^T L)^{-1} A^T b \tag{1.20}$$

Thus, solving the above equation will provide an approximate surface spanning the dimensions of an image with missing data. Higher values result in more bias in the final solution, while smaller values reduce the bias. In the case of the generated surface, high values equate to more smoothing. Selection of this value is key to the characteristics of the desired solution.

1.4.2 L-curve Regularization Parameter Selection

Methods for selecting a regularization parameter generally fall into one of three categories, a-priori, a-posteriori and heuristic (error-free) methods [58]. The first two require a measure or estimation of error in the data, which is not easily attainable with the many factors affecting MRI signal. The L-curve proposed by Hansen [59] is a widely used error free method, requiring no predetermined error values. It relies on two values which vary with the regularization parameter λ. The semi-norm of the regularized solution (x_λ) is defined:

$$\eta = \|Lx_\lambda\| \tag{1.21}$$

This represents the error between the final solution and smoothing condition. The residual norm is defined:

$$\rho = \|Ax_\lambda - b\| \tag{1.22}$$

This represents the error between the original pixel values and obtained solution. When these two errors are plotted on a log-log plot, a L shaped curve is formed. The optimal lambda value is defined as the corner of this curve which is the point of maximum curvature [60]. Curvature is defined as:

$$\kappa(\lambda) = \frac{\rho'\eta'' - \rho''\eta'}{(\rho')^2 + (\eta')^2)^{3/2}} \tag{1.23}$$

Essentially, this results in a solution which serves as a balance between error in the original data and over-smoothing from regularization errors.

1.4.3 Lung Masking

As mentioned in section 1.3.3, if quantification of lung water is desired then so to is a defined lung region (which excludes major vasculature, skeletal muscle, and

the liver). Examining an image and manually drawing an ROI to define a lung region is very straightforward but tedious. In the case of full 3D scans, manual segmentation of the entire lung is unpractical. This also introduces unwanted error from inter observer variability. Automated lung masking is necessary for practicality and quantitative consistency, but segmentation methods for lung MRI have not been established.

Threshold based methods are a common approach to any segmentation task, being fast and easy to implement. The lungs present the opportunity to use a threshold based method due to the contrast between the low signal, lung parenchyma regions and comparitevely bright surrounding tissues. However, a simple threshold does not account for the physical location of pixels, potentially including unwanted low signal regions such as bones. They are also sensitive to irregular "bright" lung regions or abnormalities and cannot account for the large water density gradient from the chest to the back.

A region growing method was developed to identify pixels within the lung parenchyma (Section 2.2.8). The growing is based on comparison of neighbouring pixels to the original seed point. This will includes pixels in direct contact to the original seeds, which can avoid unwanted areas. In addition, the procedure was made iterative to provide a gradually adapting inclusion criterion, as opposed to a completely fixed one, which adds flexibility to the growing process.

Chapter 2

Quantification of Lung Water Density with UTE Yarn Ball MRI

2.1 Introduction

Pulmonary edema (PE) is the accumulation of extravascular water in the lungs due to an imbalance in fluid filtration, leading to hypoxia and respiratory distress [2]. Cardiogenic pulmonary edema is a primary clinical feature and therapeutic target in acute heart failure [7] and is associated with the defining feature of reduced exercise capacity in heart failure [61]. Current tests used for the evaluation of pulmonary edema are qualitative (auscultation and lung x-ray), invasive (thermodilution) or require ionizing radiation (CT) [18, 12]. MRI has been shown to have the potential to quantify lung water content, with good agreement to gravimetric tests in animal studies [29, 30, 31, 32]. However, practical MRI evaluation of lung water content (lung water density, LWD) must address the constraints of low proton density (low signal to noise ratios), large magnetic susceptibility gradients that result in short T2* values (<1 ms at 3T [21]), cardio-respiratory motion [62], a large required field of

view, and the need for a signal reference. Additionally, pulse sequence design should ensure minimal T1-weighting, where elevated T1 values with increased water content [23, 63] will lead to a paradoxical signal reduction in the presence of T1-weighting. Finally, the targeted patient groups have difficulty with breath-holding and extended supine positioning due to pulmonary congestion or compliance (children) necessitating fast patient-friendly exams.

Pulse sequences with sub-millisecond ultra-short echo times (UTE) have been shown to address the effects of short lung T2* [64, 65] with applications in emphysema [66], COPD [67], perfusion [68] and imaging of lung water density [35, 38, 42]. Despite the considerable SNR improvement in the lung parenchyma with UTE acquisitions, the required center-out k-space trajectories, most commonly 2D or 3D radial, suffer from poor k-space sampling efficiency leading to exceedingly long scan times or the use of k-space undersampling, which can give rise to unwanted artifacts [50, 69]. Designer k-space trajectories have been shown to offer improved efficiency as compared to radial trajectories for lung imaging, but with relatively low reported signal to noise ratios in the lung and with significant T1-weighting [42]. Alternatively, spin-echo approaches address the limitations of short T2* values in the lung parenchyma [70], but with unwanted T2-weighting and potential sensitivity to motion and flow artifacts.

The goals of the current study were to illustrate the application of a novel efficient Yarn-Ball (YB) UTE k-space trajectory in combination with an optimized pulse sequence design and an automated image processing procedure for fast and quantitative imaging of water density in the lung parenchyma.

2.2 Methods

This study was approved by the University of Alberta Health Research Ethics Board and written informed consent was given by all study participants. Imag-

ing studies were performed on sponge phantoms for validation and illustrated in-vivo in ten healthy volunteers (age 21–50, 6 men, and 4 women).

2.2.1 Yarn-Ball (YB) k-Space Acquisition

Yarn-Ball (YB), as described in section 1.3.5, is a 3D UTE k-space sampling approach designed for acquisition efficiency [46]. Beginning center out, trajectories "wind" around the center of k-space, as opposed to projecting straight outward. This serves to improve the k-space coverage of an individual trajectory in the outer regions of k-space, where normal 3D radial sampling becomes most sparse. A YB sequence was optimized for adult lung imaging.

Trajectory design criteria included specification of field of view (FOV), spatial resolution, readout duration and maximum gradient slew rate. All YB trajectories were designed for an isotropic spatial resolution of 2.5 mm to enable both identification and removal of the larger conduit blood vessels and to provide sufficient signal to noise ratios in the lung parenchyma (<10:1 in all regions was targeted). The non-linear YB trajectories have a non-uniform point-spread-function (PSF) that offers an expanded FOV in one preferred direction (Fig. 2.2). For all studies, the expanded FOV was employed in the right-left direction, to minimize potential aliasing from the arms, which may extend to the full 60 cm inner bore width in larger subjects. The YB trajectory arms (Fig. 2.1A) were employed in a spoiled gradient-echo acquisition scheme. An asymmetric excitation pulse enabled slab-selective excitation (Fig. 2.1B) to restrict the required imaging field of view in the head-foot direction, to minimize aliasing, while maintaining a minimum echo-time of 70μs. The final targeted FOV of 300 mm used in trajectory design was determined empirically based on the calculated patterns of aliasing for a synthetic torso with realistic dimensions (Fig. 2.2), where the goal was to minimize the appearance of undersampling artifacts within the lungs.

Optimal design also balanced the advantages of longer YB readout dura-

tions, which improve acquisition efficiency by reduction of the number of arms required for full sampling and reduced T1-weighting by increased repetitions times, versus the cost of off-resonance artifacts and broadening of the PSF from T2* decay over the readout [71, 42]. Readout durations of 1.0 ms, 1.3 ms, 2.0 ms and 3.0 ms were compared in terms of scan time and image quality (sample 1.3 ms readout trajectories are shown in Fig. 2.1). The maximum gradient slew rate used for all designs was 175 T/m/s. Finally, design criteria also addressed the need for a clinically relevant short scan time, either a breath-hold or a short free-breathing acquisition ($\sim$2 minutes or less was targeted).

Additionally, a dual-echo YB trajectory (Fig. 2.1 C and D), with the same design criteria as the single echo acquisition, was generated to evaluate the feasibility of simultaneous UTE and dark lung (longer TE) imaging. The k-space trajectory for the second echo was a designed to mirror the first but beginning at the edge of k-space and winding back in (Fig. 2.1 C). The dual-echo feature was intended to enhance automated selection of lung parenchyma via increased contrast to all other tissues, and to enable the potential detection of increased T2* of lung tissue associated with increased water content [33].

2.2.2 Image Acquisition

All scans were performed on a 3T MR system (Prisma, Siemens Healthineers, Erlangen, Germany). Signal reception was by spine and body arrays (30 total coils) to provide full torso coverage. Breath-hold (single-echo) and free-breathing (dual echo) YB sequences as well as a matched breath-hold 3D radial acquisition (conventional UTE), with identical acquisition duration as the breath-hold YB, were designed and implemented.

2.2.3 Breath Hold - Yarn Ball (YB-BH)

The acquisition parameters for the breath hold (BH) YB sequence were: TE = 0.07 ms, TR = 1.97 ms, readout duration = 1.3 ms, flip angle = 2° (slab-selective excitation of 525 mm in the head-foot direction), 6555 trajectories (sample trajectory in Fig. 2.1A), 2.5 mm isotropic resolution (1.25 mm reconstructed), scan time = 13 seconds. Gradient spoiling provided 2π phase accumulation per pixel (2.5 mm) and an increment of 50 degrees for radiofrequency phase spoiling. Experiments for the determination of optimal flip angles are described below in section 2.2.9.

2.2.4 Breath Hold - Three Dimensional Radial

Breath-held 3D radial scans were completed for all in-vivo studies to enable comparison of signal to noise ratio and image quality (artifact level) to acquisition-time matched YB-BH acquisitions. The parameters were: TE = 0.07 ms, TR = 1.62 ms, readout duration = 0.5 ms with a 5 μs dwell time, FA = 2°, 8000 trajectories, 2.5 mm isotropic resolution (1.25 mm reconstructed), scan time = 13 seconds. Gradient spoilers provided 2π phase accumulation per pixel (2.5 mm) and an increment of 50 degrees for radiofrequency phase spoiling. In order to match the 13 second YB-BH acquisition duration, there was time for 8000 projections with TR = 1.62 ms, which yielded a fully sampled field of view of 126 mm. The shorter readout duration of 0.5 ms with the radial acquisitions, as compared to the 1.3 ms used for the YB acquisition, enabled an increased number of projections within the 13 second window, to minimize undersampling artifacts.

2.2.5 Free-Breathing - Yarn Ball (YB-FB)

The free-breathing (FB) version of the YB sequence included a dual-echo acquisition (Fig. 2.1 C and D) and retrospective gating for image reconstruction.

The parameters were TE_1 = 0.07 ms, TE_2 = 2.79 ms; TR = 3.54 ms; readout duration = 1.3 ms per echo, FA = 2°, 7381 number trajectories (sample trajectory in Fig. 2.1C), 2.5 mm isotropic resolution (1.25 mm reconstructed) and 5 repetitions, for a 130 second scan time. All 7381 trajectories were acquired sequentially in each of the 5 repetitions. Gradient spoilers provided 2π phase accumulation per pixel (2.5 mm) and an increment of 50 degrees for radiofrequency phase spoiling. The slightly larger number of required projections for the dual-echo YB sequence, as compared to the single-echo YB, are a result of the requirement for reduced gradient slew rates and thus reduced acquisition efficiency in the transition between the first and second echo. Additional trajectories with different readout durations of 1.0 ms, 2.0 ms and 3.0 ms were designed to address the effects of readout duration on image quality. The number of trajectories for the 1.0 ms, 1.3 ms, 2.0 ms and 3.0 ms readouts were 11935, 7381, 4465 and 2628, with relative total acquisition times of 1.34, 1.0, 0.84 and 0.69, respectively, as compared to the 1.3 ms readout case.

For all free-breathing acquisitions, the trajectories were ordered in a golden ratio pattern (section 1.3.5) to promote uniform coverage of k-space even with retrospective selection of k-space data using a respiratory navigator, as detailed in the following section.

2.2.6 Retrospective Respiratory Gating for Free-Breathing Acquisitions

Free-breathing YB scans used 5 identical sequential repetitions of the fully-sampled double-echo YB sequence. Repeated acquisitions enabled retrospective selection of a single best end-expiration acquisition for each YB arm, using a method similar to Tibiletti et al. [50]. Specifically, the magnitude of the center point of k-space acquired in each YB arm, which reflects the total image signal intensity, was used to generate a gating signal based on the change in total

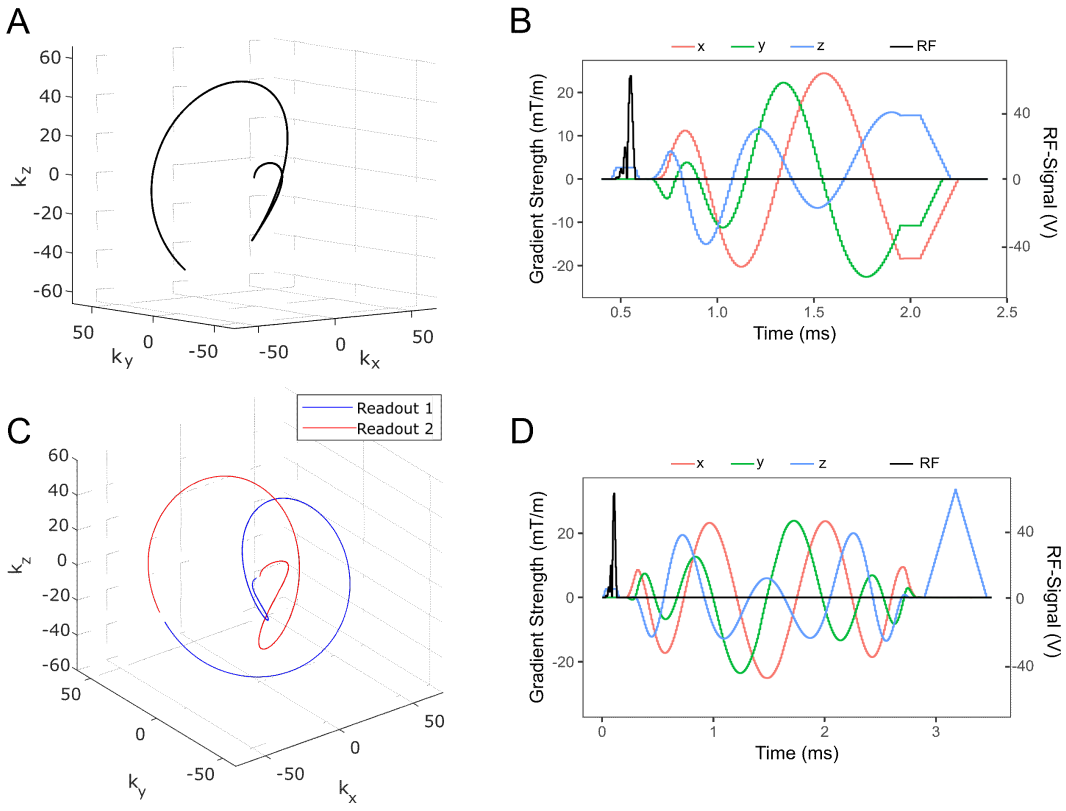

Figure 2.1: Sample yarn ball k-space trajectories. **(A)** Single-echo yarn ball k-space trajectory and **(B)** the corresponding gradient waveforms. **(C)** Dual-echo yarn ball k-space trajectories and **(D)** the corresponding gradient waveforms. The asymmetric excitation radiofrequency pulse is shown.

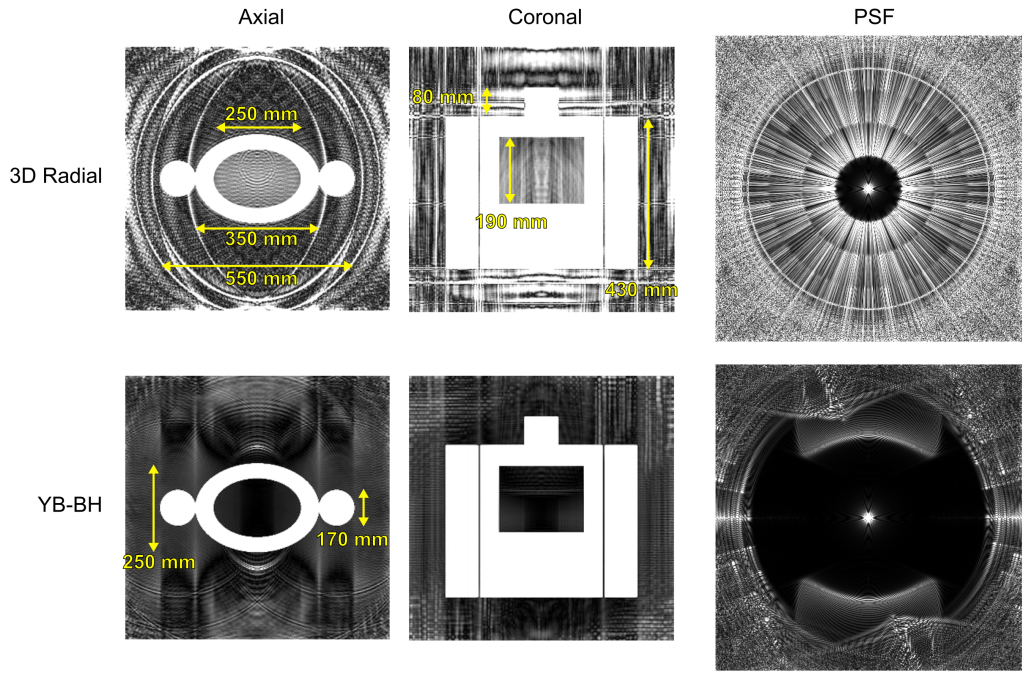

Figure 2.2: Numerical simulations of aliasing artifacts for 3D radial (8000 projections) and yarnball k-space trajectories (6555 projections) using a synthetic torso phantom. All trajectories are identical to those used for breath-hold in-vivo studies. All images are window-leveled to 25% of the intensity of the torso phantom signal level. Aliasing artifacts in the lung-region (central black space) were significantly larger with radial trajectories, with an average value of 13.3% of the solid tissues with a 100% signal intensity and versus 2.2% signal contamination for the Yarn-Ball trajectory. The point spread function images (PSF) are also displayed, where the 3D radial PSF shows a 125 mm FOV (spherical) without aliasing. The YB sequence displays an approximately 300 mm FOV in the top-bottom and in-out directions, but an expanded FOV of 450 mm in the left-right orientation.

image intensity as a function of the change in lung volume with respiration, over the entire acquisition (Fig. 2.3A). A band pass chebyshev type II filter centred around the range of potential respiratory frequencies was applied to smooth the gating signal (Fig. 2.3B). Forward-backward filtering was applied for zero phase-delay. To account for the distinct variation in the signal intensity changes from respiratory motion at each receiver-coil location, waveforms from all 30 receiver coils were combined by principle component analysis to reflect respiratory position in a single waveform (Fig. 2.3C). For each of the 7381 YB acquisition arms, a single arm from the 5 repetitions falling nearest to end-expiration was collected to form a single complete data set (Fig. 2.3).

2.2.7 Signal Reference and Spatial Normalization

The proposed method for lung water density (LWD) estimation is based on measurement of the relative signal intensities of the lung parenchyma to all surrounding solid tissues, including skeletal muscle, liver, myocardium and the blood pool, yielding relative lung water density, rLWD. All reported values from either multiple-pixel regions or the whole lung were the average of rLWD values from the individual pixels in the considered regions. The water densities for the reference tissues are assumed to be similar, with values ranging from 70%-80% [53, 54, 55]. Pulse sequence parameters were selected to minimize T1- and T2*-weighting to avoid bias in rLWD based on lung or reference tissue relaxation parameters.

The primary technical challenge for the calculation of rLWD was the measurement and correction of the effects of the spatial inhomogeneity of the radiofrequency (B_1) transmit and receive fields, within both the reference tissues and the lungs. The proposed solution was to generate a subject-specific normalization map by fitting a low spatial frequency surface to the signal intensities of the reference tissues, excluding the lung tissues. The references tissues were assumed to have a single similar uniform proton spin density. The resulting

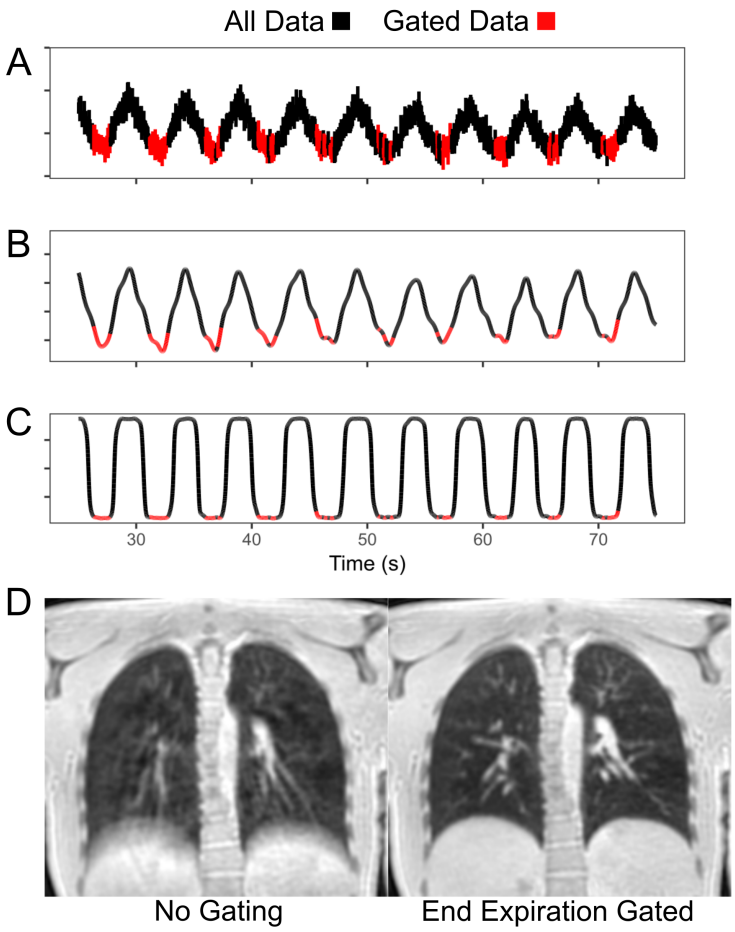

Figure 2.3: Free breathing self-navigator processing. **(A)** The central k-space value from all trajectories over free-breathing acquisition, from a single back coil. **(B)** The waveform in (A) after band pass filtering. **(C)** The waveform generated after combining the waveforms from all coils using principle component analysis. Trajectories acquired at end-expiration, as identified from the waveform in (C) are combined to form a single set complete set of k-space. **(D)** Sample reconstructed YB images with and without application of the respiratory navigator.

best-fit surface was extended over the entire torso including interpolation to within the lung regions. Following the normalization process, the reference tissues would ideally have uniform unity signal intensities and the resulting lung signal intensities (rLWD) would thus be in units of a fraction of the signal intensity in the reference tissues.

Fitting of the background signal intensity variations used regression analysis and Tikhonov regularization (based on D'Errico's Gridfit [56]). The applied Tikhonov matrix was in the form of a second order finite difference approximation, which limits slope changes and enforces smoothness, and allows the surface to span large missing regions of data (lung tissue). The regularization parameter determined the weight of this smoothing condition and was chosen with the L-curve method [60].

The predominant signal variations were in the chest to back direction due to the use of the spine and chest coil arrays for signal reception. Fitting of the background signal variations on a two-dimensional slice by slice basis in the coronal orientation was used to minimize signal variations over space and enable limitation of the best-fit surface to relatively low spatial frequencies, to mitigate overfitting. Raw images were manually cropped in the coronal orientation prior to background fitting to exclude the arms.

2.2.8 Lung Parenchyma Segmentation

Segmentation of lung parenchyma, for calculation of rLWD, utilized a custom iterative three-dimensional (3D) region growing algorithm. The goal was to exclude larger conduit vessels, solid tissue surrounding the lungs and large air spaces. The large expected gradient in lung parenchyma signal intensities from chest to back preclude the use of simple thresholding to identify lung parenchyma, even following signal normalization to correct for B1 related signal intensity variations. The iterative algorithm was initiated with a set of user selected seed pixels from within the lung parenchyma (with values falling

around 0.2 to 0.35 due to the spatial normalization process preceding masking). The growing region included new pixels based on a signal intensity acceptance window around each seed point. Specifically, the acceptance window included connected pixels (three-dimensions) that fell within a user-specified range (±((seed)/60+0.01)) around the seed pixel signal intensity. In subsequent iterations, a new set of seeds were randomly selected (one per coronal slice) from the expanded pool of accepted pixels, with a subset of these (including more near the front and back of the lungs) being supplied to the next iteration to minimize redundancy. The process was repeated automatically until an iteration adds fewer new pixels than a user-specified threshold.

2.2.9 T1 Phantom – Flip Angle Optimizations

A phantom containing 5 tubes with a wide range of T1 values (T1 = 1014, 1187, 1426, 1767 and 1992 ms) was imaged with the free breathing YB sequence, with identical parameters to in-vivo studies, to determine the effective T1-weighting at different flip angles varying from 0.5:0.5:5.0 degrees. The goal was to identify an excitation flip angle that provide a balance between acceptable signal yield and minimal T1-weighting. Images at each flip angle were normalized to the 0.5 degree flip angle image, which was assumed to have negligible T1-weighting (<2% over the range of phantom T1 values), based on expected T1-dependence of an ideal spoiled gradient echo acquisition [28]. T1-weighting with increasing flip angle was then evaluated as the relative loss in signal intensities as a function of T1 and flip angle. Relative signal yield and T1-weighting from the phantom experiments were compared to the ideal steady-state spoiled gradient-echo values, based on the assumption of perfect spoiling in each TR [28]. As an illustrative example, the signal-loss from T1-weighting, as a function of increasing flip angle, was also calculated for a specific case of a substantial increase in T1, from 1200 ms to 1700 ms, to emulate the presence of severe edema [63, 23].

2.2.10 Sponge Phantom – Validation of Water Density Quantification

Similar to the process described in Molinari et al. [33], a sponge phantom was used to verify the water quantification process using the optimized YB pulse sequence. The small air spaces within sponge materials mimic the structure and short T2* values of lung parenchyma. A 5 x 5 x 2 cm (50 ml) cellulose sponge with water volumes (water densities) varying from ∼10% to ∼60% in steps of 10% were tested. The dry weight and wet weights of the sponge for each water density were measured to determine the true water volume and thus average water density = water volume / sponge volume. For MRI experiments, the sponge was placed in an air tight container, which was immersed in a water bath. The external water bath was used as a signal intensity reference for water density quantification, similar to the methods proposed for use in the lungs. The water in the reference bath and sponge was doped with gadolinium contrast agent (Gadovist; Bayer HealthCare Pharmaceuticals, Montville, NJ) to achieve a T1 of ∼1250 ms. The breath-hold YB trajectory, with the same pulse sequence parameters used for in-vivo studies, was used to image the sponge phantom. In order to measure T2*, acquisitions were repeated over a range of TE values, with TR fixed to accommodate the longest TE used (TE = 0.07, 0.30, 0.50, 0.75, 1.0, 1.5, 2.0, and 3.0 ms; TR= 4.9 ms). Calculation of relative water density in the sponges used the spatial-normalization approach described in above, which for the sponge experiments included the water bath region surrounding the sponge as the reference (100% water density). The total calculated water volume (ml) for each sponge phantom was calculated as the sum of the normalized signal intensities multiplied by the individual voxel volumes. Mean sponge T2* was used to correct for signal decay at the minimum 0.07 ms echo time.

2.2.11 Volunteer Studies

All ten volunteers were scanned with the YB-BH, YB-FB and 3D radial sequences. For all subjects, volunteers exited the scanner after an initial image acquisitions and were then repositioned and rescanned for test-retest reproducibility. For the YB acquisitions, images were normalized to relative signal intensity units (rLWD) and the lung parenchyma was segmented as describe above. Total lung volume was determined from an expansion of the lung parenchyma mask which includes the vasculature. rLWD was evaluated in all subjects using the whole lung parenchyma average and regional rLWD was extracted by segmenting each lung into 10 slabs of equal volume, independently for head to toe, right to left, and chest to back directions. The test-retest data was evaluated by comparing whole lung values using the intraclass correlation coefficient (ICC). Chest to back slab values were also evaluted with ICC to evaluate any regional gradient changes in the test-retest data. SNR was evaluated on a pixel by pixel basis using the method described by Kellman and McVeigh [52]. SNR, image quality and the presence of artifacts was compared between the YB-BH, YB-FB and 3D radial sequences.

2.3 Results

2.3.1 Sponge Phantom

The sponge phantom experiments illustrated strong linear agreement between the water density (%) measured by direct wet weights of the sponges and water volume derived from YB experiments ($y = 1.06x + 0.81$, x = 9.3 to 55.4%, $p<0.001$, $R^2 = 0.99$, Fig. 2.4). A similar linear relationship exists without T2* correction, but with minor systematic underestimation of water volume, as expected. The median sponge T2* was 0.94 ms (interquartile range = 0.85 ms – 1.20 ms).

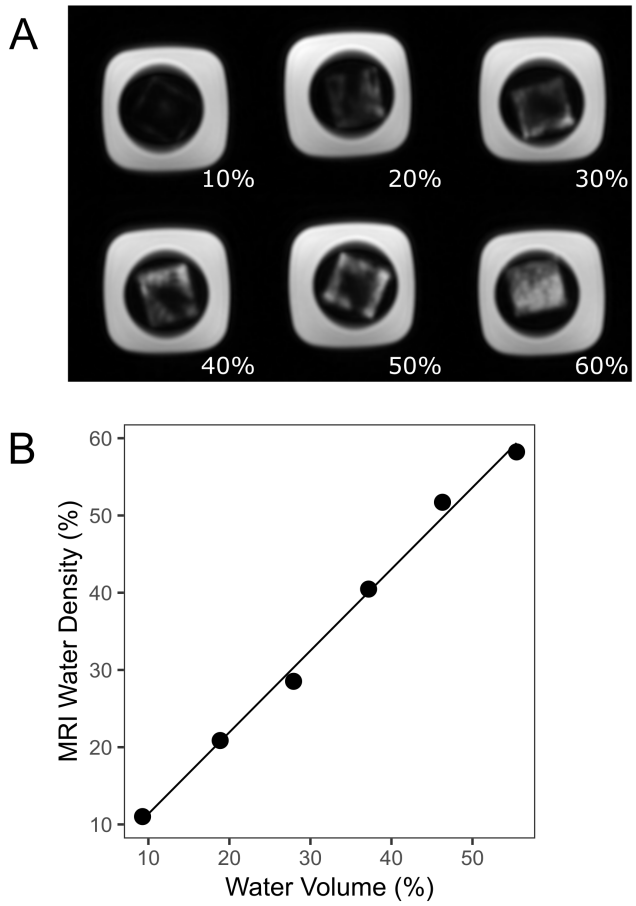

Figure 2.4: Sponge phantom results. **(A)** Sample YB images from the six different sponge experiments. **(B)** Strong agreement was measured between the MRI derived water content and gold standard wet weight ($y = 1.06x + 0.81$, $x = 9.3$ to 55.4%, p<0.001, $R^2 = 0.99$).

2.3.2 T1 Phantom

Significant T1-weighting was observed as a relative reduction in signal yield in the longer T1 tubes with increasing flip angles, as expected (Fig. 2.5). Compared to the minimum flip angle of 0.5°, which yields negligible T1-weighting, the selected optimal flip angle of 2° yielded 3.35 times more signal on average, for the T1 values considered (∼1000 to 2000 ms). Larger flip angles offered only moderate increase in signal yield over the 2° acquisitions, to a maximum of 4.1 times more than 0.5° (on average), but with significantly more T1-weighting. Predicted signal yields using ideal spoiling and steady-state conditions were similar to experimental values, with slightly less T1-weighting (Fig. 2.5B). Using these signal intensity relationships (Fig. 2.5B), the percent signal loss from T1-weighting between T1 = 1200 ms vs. T1 = 1700 ms was 5.4% for a 2° flip angle and 13.7% at 4° (Fig. 2.5C), with similar relationships for empirical and predicted T1-weighting.

2.3.3 Signal Reference and Spatial Normalization - Healthy Controls

An illustration of background signal normalization of a YB acquisition displays the typical signal intensity variations in the coronal slice orientation (Fig. 2.6A), masking to identify tissue regions included in the normalization process (Fig. 2.6B), the resulting best-fit normalization map (Fig. 2.6C) and the final intensity corrected image (Fig. 2.6D). This process was repeated, independently, for all coronal slices. The corresponding pre-normalization and post-normalization images from sagittal and axial views, for the same subject, illustrate the uniform signal intensity, in three dimensions, following correction (Fig. 2.6 E-H). Signal intensity profiles through the lungs and surrounding reference tissues highlight the uniform 100% signal intensity in all reference tissues (Fig. 2.6 I-K). Similar results were observed for all 10 subjects.

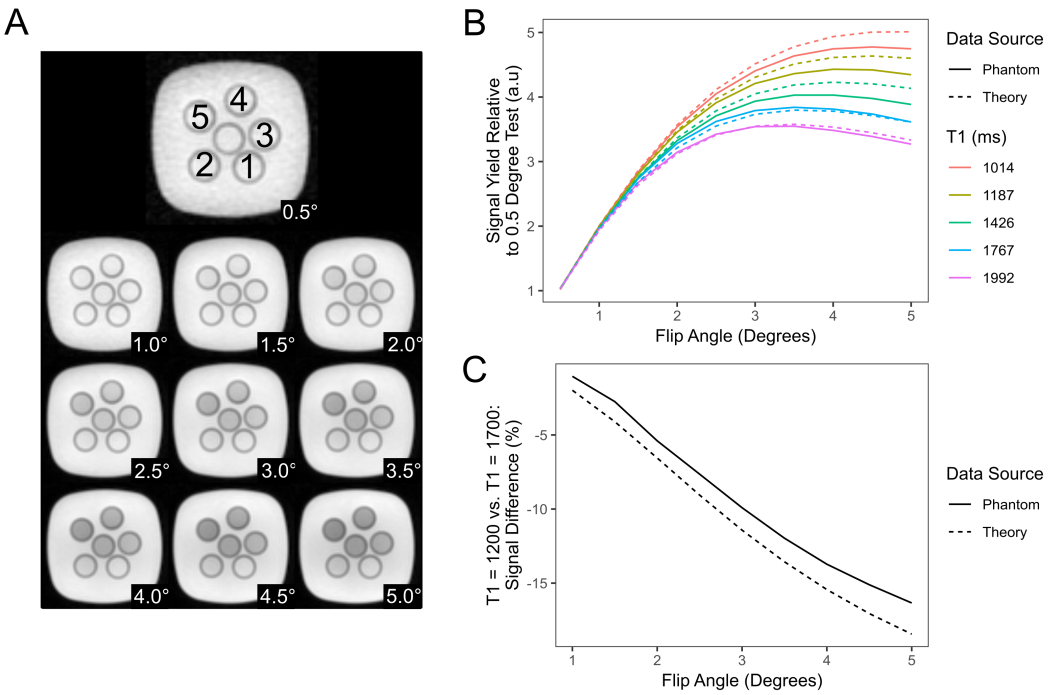

Figure 2.5: **(A)** YB-FB images of a T1 phantom for flip angles of 0.5° to 5°. 5 outer tubes were examined, numbered by increasing T1 (1 = 1014 ms, 2 = 1187 ms, 3 = 1426 ms, 4 = 1767 ms, 5 = 1992 ms). **(B)** Relative signal yield, normalized to the 0.5° acquisition, as a function flip angle for the 5 outer tubes (phantom experiments - dashed lines, theory based – solid lines). **(B)** Using the data in B), the percent difference in signal between subjects at T1 = 1200 ms and T1 = 1700 ms.

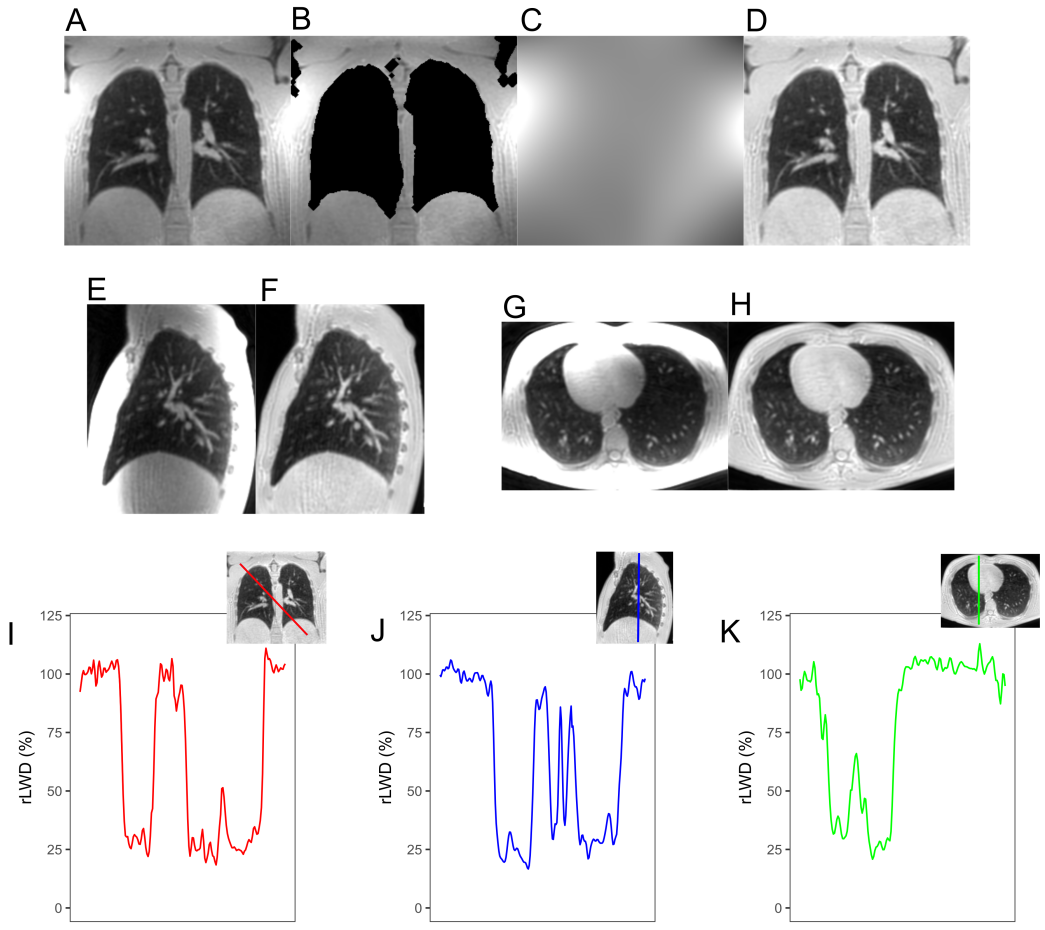

Figure 2.6: Background signal intensity correction approach. **(A)** Uncorrected coronal slice. **(B)** Masking to include reference tissues surrounding the lungs. **(C)** Best-fit surface generated from image in B) with regression and tikhonov regularizaiton. **(D)** Normalized image from A) after division by the best-fit surface from C). Sample sagital and axial views of the same subject before and after normalization are shown in **(E) - (H)**. **(I) - (K)** Sample signal intensity profiles from intensity-corrected images in coronal, sagittal and axial views, respectively.

Illustrative 3D radial (breath-hold) and YB-BH images are shown for four subjects (Figure 2.7). All acquisitions were 13 seconds in duration and the same signal normalization process was completed in all cases. From all ten subjects, SNR values were similar for breath-hold radial and YB acquisition approaches, and also for the free-breathing YB acquisition (Table 1), with SNR > 10 in all regions. However, radial images showed significant streaking artifacts due to undersampling while no artifacts were visible in the YB images, with similar results in all ten volunteers.

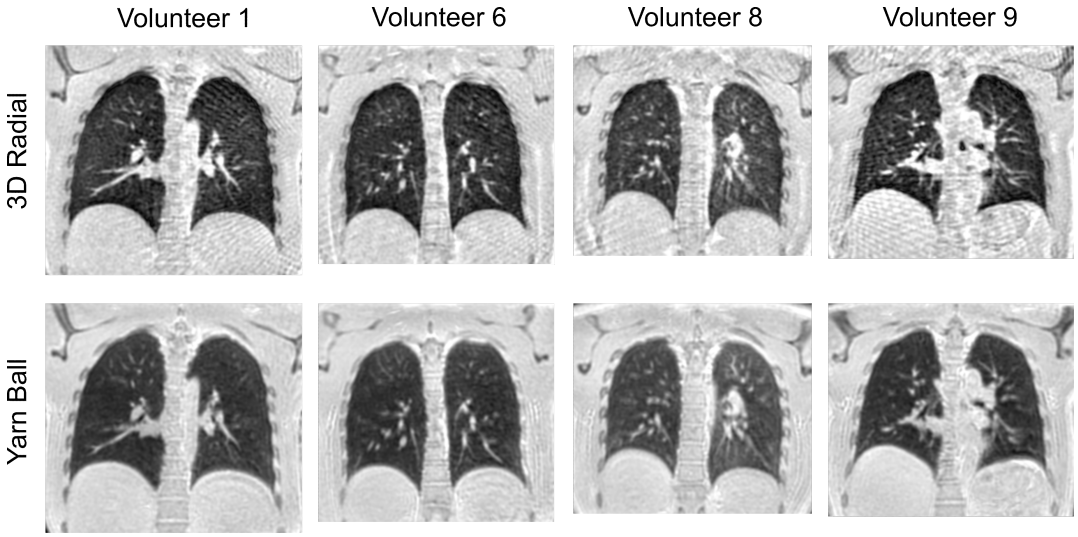

Figure 2.7: Comparison of normalized 3D radial and YB-BH images from matched 13 second acquisitions in four volunteers. The 3D radial images (top) suffer from streaking artifacts due to undersampling.

2.3.4 Retrospective Respiratory Gating for Free-Breathing Acquisitions – Healthy Controls

Sample free-breathing YB images, with and without the application of respiratory navigators, illustrate the clear improvement in image quality with selection of data acquired at end-expiration (Fig. 2.3D). Similar results were observed in all 10 subjects. Free-breathing images for both echo times (TE = 0.07 ms and 2.79 ms) from four representative subjects further illustrate the typical free-

breathing image quality with the use of the respiratory navigators (Fig. 2.8). The longer echo images highlight the short T2* of the lung parenchyma, with similar breath-hold-like image quality. SNR in the free breathing scans were similar to the breath hold acquisitions (Table 2.1). Lung parenchyma signal intensity in the longer TE images was similar in intensity to the background noise level in all volunteers in all slices and all locations.

SNR	Front	Center	Back
3D Radial	11.5 ± 3.0	11.6 ± 2.6	19.5 ± 3.4
YB Breath Hold	11.9 ± 1.4	11.1 ± 1.7	20.2 ± 3.6
YB Free Breathing	13.2 ± 2.1	10.6 ± 2.0	19.1 ± 4.0

Table 2.1: SNR Results for All 10 Volunteers

2.3.5 Optimization of Acquisition Duration – Healthy Controls

Increasing YB readout duration over a range of 1.0 ms to 3.0 ms increased acquisition efficiency (reduced acquisition time) by a factor of 1.94, but at the price of reduced image quality (Fig. 2.9). The 1.3 ms readout duration yielded similar image quality as the 1.0 ms readout on visual inspection but with ∼30% increase in acquisition efficiency. The longer 3.0 ms readout improved efficiency an additional 30%, but with a more marked reduction in image quality. Also, for the expected T2* = 0.7 ms for the lung parenchyma at 3.0T, the 3.0 ms readout would be expected to yield significant blurring of the parenchyma. Readout durations of up to 2·T2* has been shown to be acceptable for lung tissue [42], supporting a readout duration of 1.3 ms.

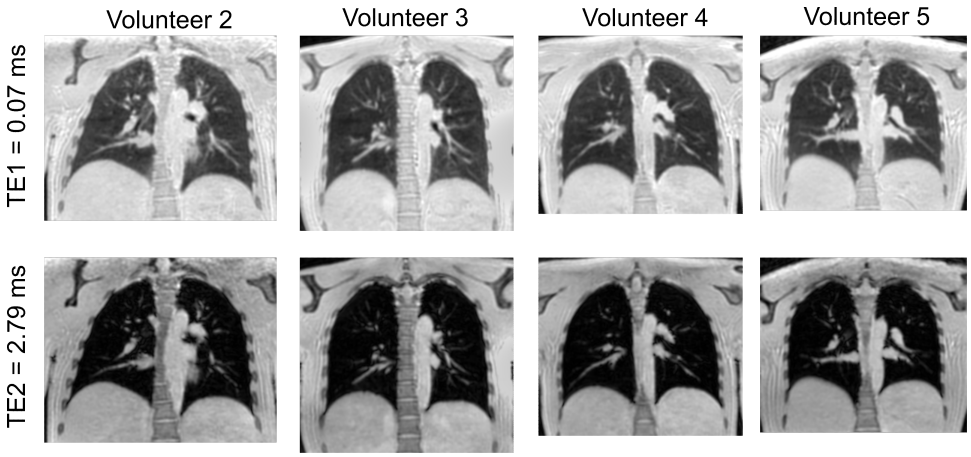

Figure 2.8: Normalized free breathing dual-echo YB images from four volunteers with retrospective gating at end-expiration. All images have identical window levels.

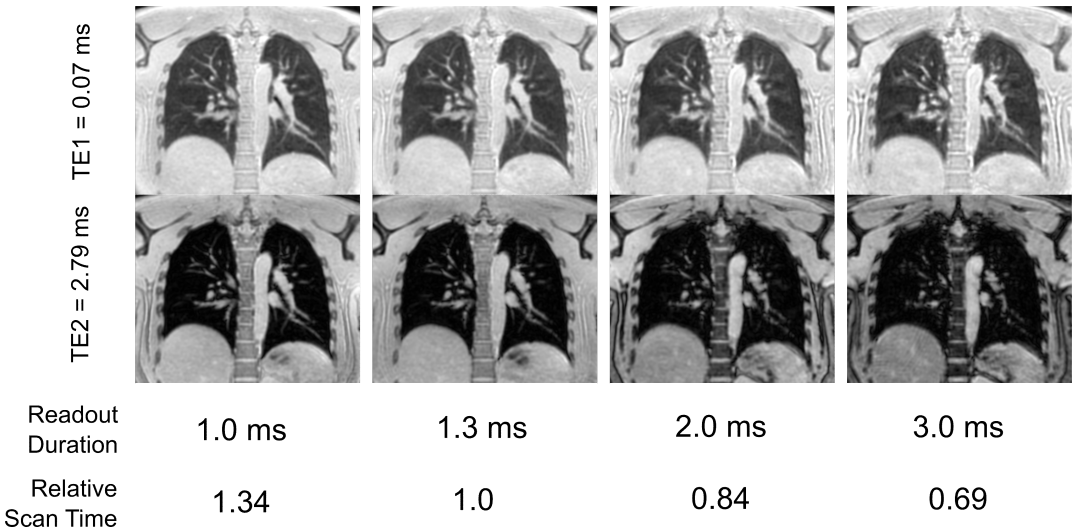

Figure 2.9: First and second echo images from YB-FB acquisitions for increasing readout durations in four volunteers. Blood vessel sharpness erodes and image artifact levels increase with increasing readout duration, with similar image quality in 1.0 ms and 1.3 ms readouts.

2.3.6 Image Segmentation and Lung Water Density – Healthy Controls

Three-dimensional lung masks were generated for each subject using the region growing algorithm to identify pixels within the lung parenchyma (Fig. 2.10A). Average relative lung water density (rLWD) and lung volumes from YB-BH and YB-FB scans, from the repeated acquisitions, illustrate the similar values with the two acquisition methods, and similar consistency between repeated scans (Fig. 2.10 B and C). Reproducibility of whole lung rLWD yielded ICC3 = 0.93 for breath-hold ($p < 0.001$) and ICC3 = 0.87 for free-breathing studies ($p < 0.001$). Total lung water signal had higher ICC values for both breath-hold (ICC3 = 0.99) and free-breathing acquisitions (ICC3 = 0.99), likely because total water content is less sensitive than water density to the extent of lung inflation.

Regional variations in rLWD were evaluated by segmenting the lung into 10 equal volumes, independently, along each axis (Fig. 2.11). A significant chest to back gradient in rLWD was observed in all volunteers (Fig. 2.11C), similar to previous studies [72]. Lung water values did not vary considerably in the head to foot direction (Fig. 2.11A), but with elevated values in the left lung, towards the heart (Fig. 2.11B). Chest to back lung slab rLWD showed high ICC values (breath hold ICC3 = 0.97, $p < 0.001$, free breathing ICC3 = 0.96, $p< 0.001$), showing no changes in chest to back gradients between scans.

2.4 Discussion

An optimized UTE yarnball k-space trajectory yielded 3D lung images with short patient-friendly acquisition times (13 second breath-hold or 2 minutes of free breathing with a dual-echo acquisition). Both breath-hold and free-breathing yarnball sequences provided good lung SNR (ranging from 10:1 to 20:1) with a low (2°) flip angle designed to minimize T1-weighting, a short

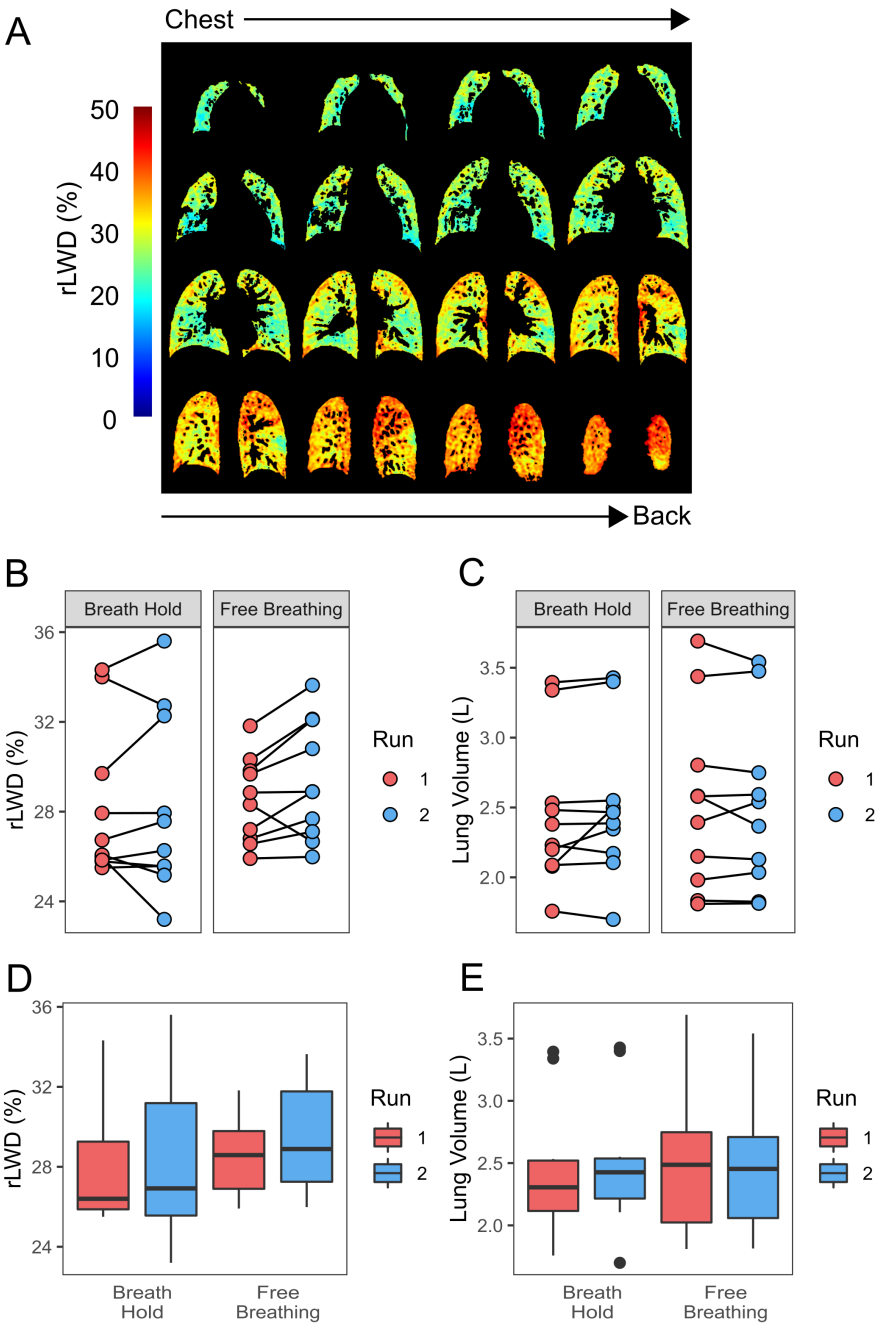

Figure 2.10: **(A)** Sample relative lung water density (rLWD) images from a volunteer from a YB-FB acquisition. 16 of 124 coronal slices covering the chest are shown. **(B)** Individual volunteer rLWD values for the breath-hold (YB-BH) and free-breathing (YB-FB) experiments, for the two repeated acquisitions (connected lines). **(C)** Corresponding total lung volumes. Box plots summarize average values for rLWD in **(D)** and lung volumes in **(E)** from all 10 volunteers.

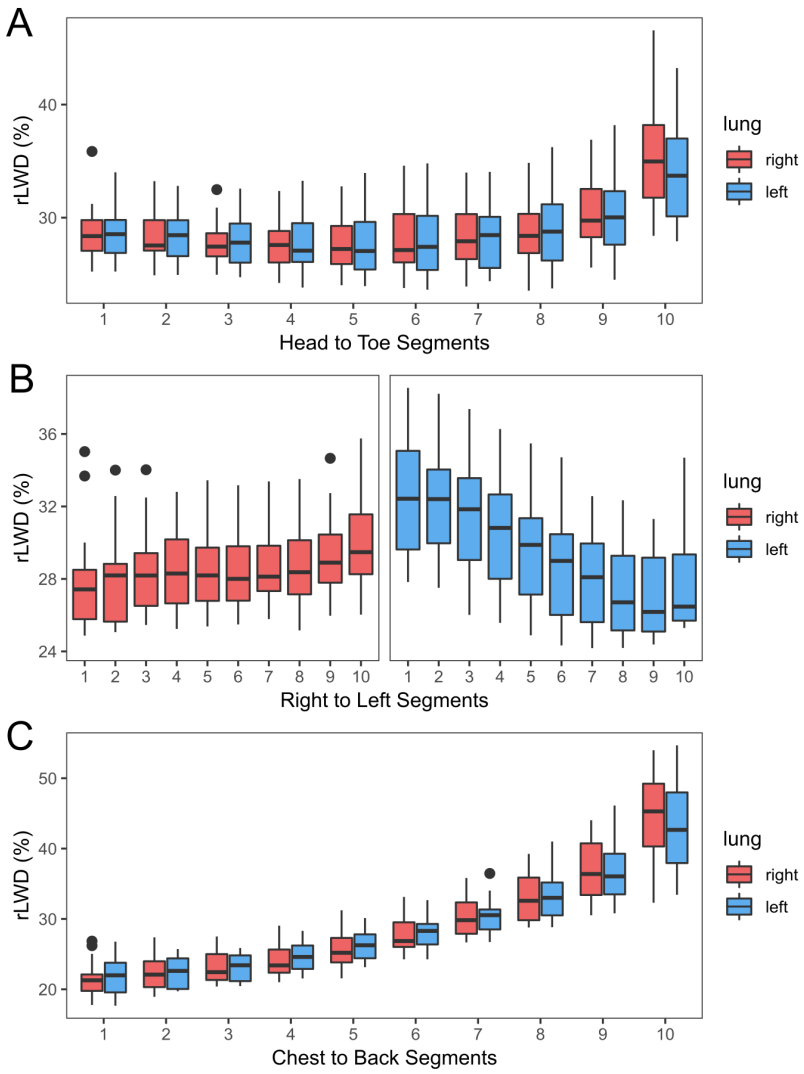

Figure 2.11: Regional rLWD values when segmented into 10 slabs of equal volumes along different orientations: **(A)** Head to toe, **(B)** right to left, and **(C)** chest to back. Data included from all 10 healthy volunteers (YB free breathing).

TE = 70 μs for minimal T2*-weighting, sufficient spatial resolution to exclude larger conduit vessels and with minimal undersampling artifacts. In contrast, a conventional radial image acquisition, matched to the YB scan time, had significant undersampling artifacts as a result of the lower efficiency of the radial trajectory, with a smaller 126 mm fully-sampled field of view.

Further scan time reductions are possible with the use of longer readouts, however an optimal readout duration of 1.3 ms was identified based on the expected lower-end of T2* values at 3.0T of 0.7 ms. The expected minor loss of SNR and blurring of the lung parenchyma with readouts durations $\sim$2$\times$T2* were considered acceptable [42]. Longer readouts were associated with the emergence of minor off-resonance artifacts.

Calibration of the absolute signal intensities into relative lung water density by normalization to all surrounding solid tissues (heart and the blood pool within, liver and other abdominal organs and skeletal muscle) yielded consistent results in volunteers, with validation in sponge phantoms with in-vivo-like T2* values (<1ms). While previous UTE studies designed to measure lung water have used larger flip angles to maximize signal yield [42], a noted assumption was similar lung and reference skeletal muscle T1 values. This assumption precludes the use of other reference tissues with different T1 values (liver, blood, myocardium) and does not address the expected increases in lung T1 in the presence of edema [23, 63]. Other studies have incorporated a skeletal muscle signal reference to estimate lung water density [35], but also did not account for T1-weighting or the significant transmit and receive B1 field inhomogeneity. In the current study, the use of all solid tissues as a signal reference also enabled simultaneous correction of B1 transmit and receive inhomogeneity.

The process developed for selection of the background tissues, for the signal normalization and correction of B1-inhomogeneity was largely automated, as was the region growing algorithm used to identify pixels within the lung parenchyma, following normalization. Lung water density depends strongly on

lung inflation due to the displacement of tissue by air. Breath-hold consistency is thus a potential large source of bias in the measurement of rLWD, and even short breath-hold maneuvers can be challenging for patients with pulmonary congestion. A two minute free-breathing variation of the yarnball approach yielded breath-hold image quality in all subjects with excellent reproducibility, and would thus offer a more patient-friendly approach. The proposed free-breathing acquisitions used a constant 5 image repetitions to ensure the acquisition of end-expiration respiratory phases for all k-space data. Prospective gating would likely increase efficiency considerably, however the current scan time of two minutes is not prohibitive. Considerable time savings could also be achieved by a modest reduction in spatial resolution (e.g. an increase from 2.5 mm to 3.2 mm resolution will reduce scan duration by a factor of 2), or with the application of parallel imaging [73].

It was perhaps not surprising that total lung water content, as compared to average rLWD, had superior test/re-test reproducibility, with higher ICC values. Specifically, small differences in breath-hold lung volume or lung inflation with free-breathing acquisitions will have a direct effect on water density. Interpretation of rLWD, particularly in a given individual over time, would thus ideally also include assessment of lung volume to correct for inflation effects on water density.

2.4.1 Limitations

The echo time of 70 μs used in the current study will lead to an unaccounted signal loss of $\sim$10% for a lung parenchyma T2* of 700 μs, which is the lower end of values expected at 3T [21]. While shorter T2* value would lead to a larger underestimation of rLWD, it is more likely that increased T2* values associated with edema will be encountered in clinical studies, that will lead to an increase in the acquired signal that will emphasize the presence of edema. In clinical studies, the dual echo free-breathing YB acquisition will be sensitive

to increased T2* values in the presence of edema using the longer second echo time of 2.79 ms. Another limitation is the assumption of uniform and constant tissue water density for signal referencing. While tissue water content has been measured to fall in a relatively narrow range of 70%-80% [53, 54, 55], the content does vary between tissue types and likely with pathology. However, all solid tissues have relatively high water content in health and thus have limited potential for increases in water density. In contrast, the lungs have relatively low water density in health and have an easily displaceable air component to enable large changes with pathology. Lung water content can readily double or more with heart failure [70], for example. Also, the use of a large composite of reference tissues at all locations surrounding the lungs was designed to limit the susceptibility of the normalization process to precise knowledge of water content and the associated measured signal intensity in one tissue (or external reference) at one location. External references are appealing as a known source of 100% spin density, but the potentially extreme variations in signal yield for samples outside of the body from the unavoidable B_1 and B_0 inhomogeneity, particularly at higher field strengths, can lead to excessive variability and thus were not used in the current study. Spatial resolution is also a potential limitation. The acquired spatial resolution of 2.5 mm in each dimension was proposed to be sufficient to identify and remove the larger conduit blood vessels from the lung parenchyma, however, the effects of higher spatial resolution on vessel removal and the rLWD values was not evaluated. While the automated processing was successful in all volunteers, the larger body dimensions and higher lung water content that will be present in some patients may require different parameters for similar performance. Finally, while phantom studies showed excellent agreement between gravimetic and MRI estimation of water content, the measured rLWD values have not been validated in-vivo.

Chapter 3

Discussion

UTE Yarn Ball MRI acquisitions and the accompanying image processing methods were developed to overcome the challenges of quantitative MRI of water density in the lung parenchyma. Short echo-times (70 μs) largely eliminated T2* weighting, low flip angles largely eliminated T1 weighting, and optimized acquisition efficiency enabled fully sampled three-dimensional lung images in patient-friendly scan durations (breath-hold or short free-breathing). A custom designed post-processing approach both corrected for B_1 transmit and receive inhomogeneity and yielded lung images in units of normalized spin density, relative to all solid tissues surrounding the lungs. A final automated segmentation approach enabled user-independent selection of lung parenchyma. Validation was provided in a sponge phantom with similar T2* and T1 of the lung, and consistency of lung water density values was illustrated in 10 healthy subjects.

3.1 Limitations and Future Directions

Longer readout durations improve acquisition efficiency, with faster coverage of k-space, but short T2* regions may lose significant signal by the end of the readout, which manifests as blurring in the final image. Additionally, the magnitude of artifacts from off-resonance effects are directly related to the

readout duration. A 1.3 ms readout was chosen as the maximum duration before significant artifacts appear, but the potential blurring effect on short T2* regions should still be noted.

The targeted 300 mm FOV was empirically chosen to avoid aliasing artifacts, which holds true in the majority of subjects. With traditional k-space encoding methods, a 300 mm FOV would cause aliasing leading to "phase wrap-around" artifacts, but in the case of YB sampling the aliasing results in incoherent noise throughout the image. This is often negligible, but in larger subjects this can be a significant detriment to image quality. Figure 3.1 shows the noise increase which accompanies a patient with a large torso. If this proves to be an issue in the larger healthy control scans, an increase in FOV at the cost of time efficiency would be a simple solution. Unfortunately this is not a simple linear increase, the 26 second 300 mm FOV double-echo YB scan would increase to 46 seconds with a 400 mm FOV.

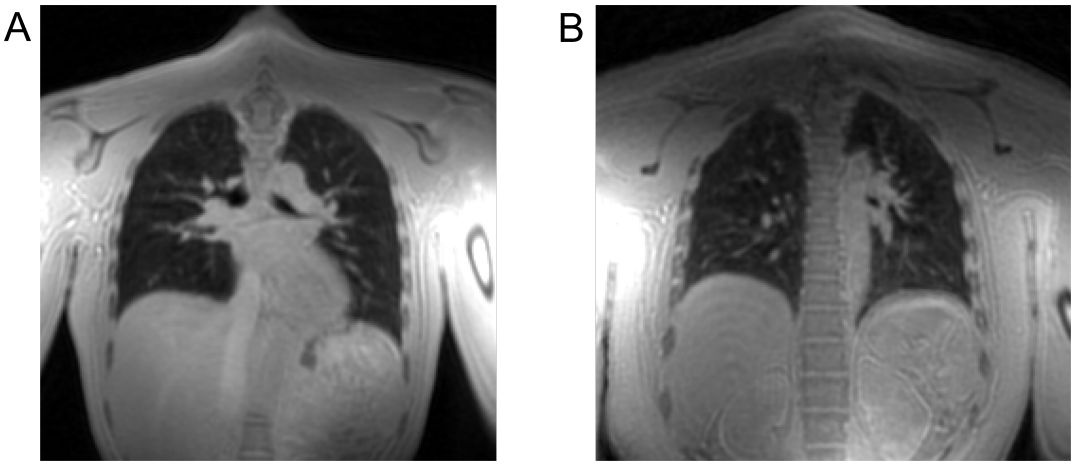

Figure 3.1: Unedited free breathing YB images showing the potential increase in noise due to aliasing between a volunteer with a small torso in **(A)** and large torso in **(B)**.

The dual-echo YB variant currently aids in image processing, as the increased T2* weighting adds contrast to facilitate tissue differentiation. Ideally, future image processing algorithms could rely solely on the original UTE image, providing the ability to remove the second echo when undesired, and shorten the

scan times by 50%. Alternatively, another potential future direction includes expanded application of the second echo image, for example the calculation of T2*. This could be determined by signal intensity loss between the first and second echo images. The readout duration would likely be shortened in this case, as lung parenchyma signal has generally been lost by the currently implemented 2.72 ms second echo time. T2* is a potential source of uncertainty, having been found to change with inflation [34] and nature of PE [74]. Lack of T2* knowledge is another limitation in the current technique. While UTE methods go a long way to mitigate T2* weighting, direct calculation of T2* would allow for more accurate proton density measurement.

Free breathing methods are essential moving forward with clinical studies. Breath holds are not only difficult and uncomfortable for patients, but also inconsistent. A specific level of lung inflation cannot be expected to be maintained across repeated scans. Free breathing techniques can remove this variable by purposely selecting for a diaphragm position or lung inflation. However, our current retrospective gating method leaves room for improvement. First, the method is based only on respiratory phase so the unique respiratory cycles of different patients, being irregular in position or period, can align poorly with scan repetitions, which complicates acquisition of a complete data set. Second, the duty cycle is quite low at 20% since only the trajectories nearest to end expiration were taken scans over 5 averages. A more efficient binning method, which extracts physical position would be beneficial. For example, a sliding window method like the "img-SG" technique proposed by Tibiletti et al. [50]. Therefore, trajectories which line up in space could be combined, leading to a more targeted and efficient retrospective gating. Lung volume variation undermines the accuracy of repeated measurements and the effectiveness in disease tracking. Reproducible, patient friendly lung volume standardization will be key to reliable lung water density calculations in longitudinal studies.

While the ideal scenario presented in the "sponge phantom" experiment

showed excellent results for quantification of water content, there are many potential pitfalls for water quantification in vivo. In addition to T2* inconsistency, some T1 weighting is still present. The low flip angle of 2 degrees mitigates this, but T1 can still vary across the lungs and could be significantly different between reference tissues which include blood, skeletal muscle and the liver. In addition, reference tissue signal T1 weighting will corrupt the normalization process. We chose to minimize flip angle but an increase to TR would be another simple solution to avoid T1 weighting, however this would necessitate time efficiency improvements elsewhere.

The current normalization process produces very consistent images, fully eliminating the large signal gradient across an adult torso normally present with chest and back coil arrays. However, this method is still only an approximation of the inherent B_1 inhomogeneities. The surface fitting method with Tikhonov regularization functions using available reference tissue information, and the L-curve method is based on balancing the error between the smoothed result and original data. No information on B_1 is directly measured or predicted. Unfortunately, such analytical determinations are impractical in vivo, so the current technique fulfils the purpose of generally correcting images with limited information. The lack of B_1 transmit and receive sensitivity information will always be a limitation in quantifying lung images in vivo.

The extremely bright chest surface arising from B_1 inhomogeneity with the use of a chest coil can also lead to other artifacts. The comparatively lower signal intensity in the more central regions causes them to be more susceptible to artifacts originating from the chest surface, from off-resonance and motion artifacts. A common manifestation of this is "ringing" or a series of streaks running parallel to the chest wall (Fig. 3.2). These artifacts were reduced with sufficiently strong gradient spoiling and were minor enough to not be of concern in lung water quantification but do visually affect image quality.

Signal quantification relies on the reference tissues surrounding the lungs

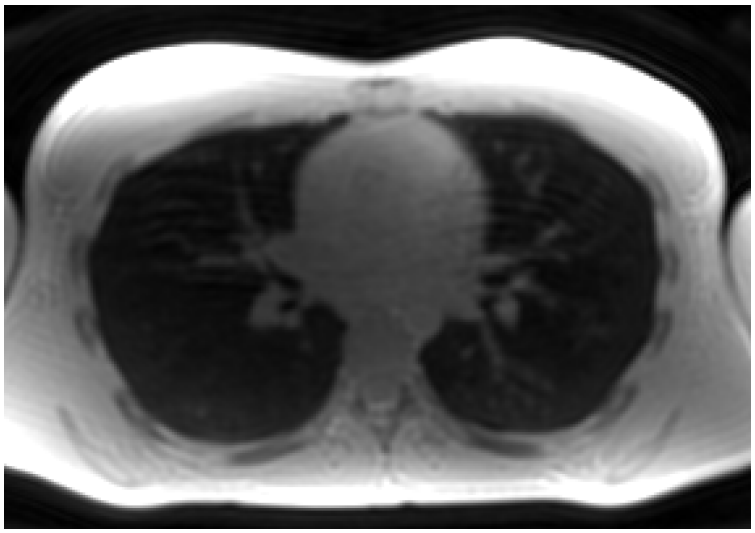

Figure 3.2: Uncorrected axial image with "chest ringing" artifacts radiating from the bright chest wall.

to be relatively uniform in proton density. The limited literature on the subject does show consistent water density between these tissues (70%-80% water density [53, 54, 55]), but more detailed information would be beneficial. This is especially important when considering the potential for increase or decrease with disease, such as the expected range of skeletal muscle water in heart failure or dialysis patients, for example, in whom edema is possible throughout the body. Nonetheless, in cases of mild pulmonary edema an increase in water content by up to 100% has been shown [70], and in severe cases of pulmonary edema an increase on the order of 250% can be expected in gravimetric results [75], meaning changes to proton density in reference tissues, which have limited potential for increase in water content, would likely be negligible in comparison. Specifically, the lungs are predominantly air, which can be easily displaced with expanding water compartments while solid tissues are already $\sim$75% water and have to displace solid materials to increase water content.

The lung masking procedure is a final key area to be improved. While good results can be obtained with the current iterative region growing method, this relies heavily on the nuanced selection of a threshold and can vary slightly due

to the random seeding process. Because of this, it remains a challenge to define consistent masking parameters that are appropriate for all subjects, which is desired for proper comparisons of signal quantity. In patients suffering from PE, this will likely be a greater issue since regions with elevated lung water density will be much brighter than healthy lung tissue. Defining what constitutes vasculature is another ambiguous factor in the masking procedure. While large blood vessels are easily excluded, drawing the line between partial volume or small blood vessels and bright lung regions is difficult. Other image processing methods and segmentation techniques should be investigated in mitigating these issues. This could include other threshold based approaches, those involving an atlas or statistical shapes, or machine learning methods [76]. Whatever the solution, full automation is desired. Inter-observer variability should be minimized for accurate quantification of lung water. For viability in clinic, a robust and fast image processing tool-kit will be needed.

Another future direction would be examining the effects of lying prone for long periods of time, an extension of the already observed gravitational effects while lying prone. Blood is expected to come up from the legs and redistribute throughout the body while lying prone, so this could lead to increased rLWD.

Finally, the increases in sampling efficiency were attained without acceleration techniques such as parallel imaging [73], compressed sensing [77] or machine learning reconstruction [78]. Adding such techniques would be an obvious first direction to take in improving YB k-space acquisitions. These gains could be used to further shorten scan times, provide larger FOVs, or increased spatial resolution. However, the achieved 2.5 mm isotropic resolution was sufficient for identification and removal of of the larger while maintaining sufficiently high SNR (>10:1) in the targeted lung parenchyma.

3.2 Conclusions

Pulmonary edema is a common condition associated with heart failure, kidney failure (hemodialysis) and several other pathologies. The defining feature is increased water content. Commonly used tests to detect edema, such as chest X-Ray, are qualitative and used primarily only to broadly categorize severity but are not appropriate to measure changes with therapy or identify sub-clincial pathology. CT imaging can be used to measure lung water content, but requires ionizing radiation, and does not distinguish water and fibrotic tissue. Other tests for lung water evaluation require injection of tracers. 3D UTE Yarn Ball MRI provides quantitative lung water density information, while being non-invasive and free of ionizing radiation. Full lung UTE images can be obtained with short scan times, overcoming that key inherent challenge of lung MRI, and automated image processing enables largely user-independent evaluation, further increasing the practicality of the approach . Looking forward, the technique could be used for routine radiological evaluation of pulmonary edema, provide a much needed quantitative endpoint for clinical trials targeting pulmonary edema, guide treatment and shed new light on the condition itself.

Bibliography

[1] Murray JF. The structure and function of the lung. *Int J Tuberc Lung Dis*, 14(4):391–6, Apr 2010.

[2] Murray JF. Pulmonary edema: pathophysiology and diagnosis. *Int J Tuberc Lung Dis*, 15(2):155–60, Feb 2011.

[3] Levick JR and Michel CC. Microvascular fluid exchange and the revised starling principle. *Cardiovasc Res*, 87(2):198–210, Jul 2010.

[4] Schraufnagel DE. Lung lymphatic anatomy and correlates. *Pathophysiology*, 17(4):337–43, Sep 2010.

[5] Ketai LH and Godwin JD. A new view of pulmonary edema and acute respiratory distress syndrome. *J Thorac Imaging*, 13(3):147–71, Jul 1998.

[6] Roguin A, Behar D, Ben Ami H, Reisner SA, Edelstein S, Linn S, and Edoute Y. Long-term prognosis of acute pulmonary oedema–an ominous outcome. *Eur J Heart Fail*, 2(2):137–44, Jun 2000.

[7] Platz E, Jhund PS, Campbell RT, and McMurray JJ. Assessment and prevalence of pulmonary oedema in contemporary acute heart failure trials: a systematic review. *Eur J Heart Fail*, 17(9):906–16, Sep 2015.

[8] Gheorghiade M, Follath F, Ponikowski P, Barsuk JH, Blair JE, Cleland JG, Dickstein K, Drazner MH, Fonarow GC, Jaarsma T, Jondeau G, Sendon

JL, Mebazaa A, Metra M, Nieminen M, Pang PS, Seferovic P, Stevenson LW, van Veldhuisen DJ, Zannad F, Anker SD, Rhodes A, McMurray JJ, and Filippatos G. Assessing and grading congestion in acute heart failure: a scientific statement from the acute heart failure committee of the heart failure association of the european society of cardiology and endorsed by the european society of intensive care medicine. *Eur J Heart Fail*, 12(5):423–33, May 2010.

[9] Roger VL. Epidemiology of heart failure. *Circ Res*, 113(6):646–59, Aug 2013.

[10] Rezoagli E, Fumagalli R, and Bellani G. Definition and epidemiology of acute respiratory distress syndrome. *Ann Transl Med*, 5(14):282, Jul 2017.

[11] Lange NR and Schuster DP. The measurement of lung water. *Crit Care*, 3(2), 1999.

[12] Assaad S, Kratzert WB, Shelley B, Friedman MB, and Perrino A Jr. Assessment of pulmonary edema: Principles and practice. *J Cardiothorac Vasc Anesth*, 32(2):901–14, Apr 2018.

[13] Patroniti N, Bellani G, Maggioni E, Manfio A, Marcora B, and Pesenti A. Measurement of pulmonary edema in patients with acute respiratory distress syndrome. *Crit Care Med*, 33(11):2547–54, Nov 2005.

[14] Gluecker T, Capasso P, Schnyder P, Gudinchet F, Schaller MD, Revelly JP, Chiolero R, Vock P, and Wicky S. Clinical and radiologic features of pulmonary edema. *Radiographics*, 19(6):1507–31, Nov-Dec 1999.

[15] Andrew Dixon. Normal ct chest. https://radiopaedia.org/cases/normal-ct-chest. Accessed: 2020-01-03.

[16] Picano E and Pellikka PA. Ultrasound of extravascular lung water: a new

standard for pulmonary congestion. *Eur Heart J*, 37(27):2097–104, Jul 2016.

[17] Cortellaro F, Ceriani E, Spinelli M, Campanella C, Bossi I, Coen D, Casazza G, and Cogliati C. Lung ultrasound for monitoring cardiogenic pulmonary edema. *Intern Emerg Med*, 12(7):1011–7, Oct 2017.

[18] Jozwiak M, Teboul JK, and Monnet X. Extravascular lung water in critical care: recent advances and clinical applications. *Ann Intensive Care*, 5(1), Dec 2015.

[19] Mihm FG, Feeley TW, and Jamieson SW. Thermal dye double indicator dilution measurement of lung water in man: comparison with gravimetric measurements. *Thorax*, 42(1):72–6, Jan 1987.

[20] Schenck JF. The role of magnetic susceptibility in magnetic resonance imaging: Mri magnetic compatibility of the first and second kinds. *Med Phys*, 23(6):815–50, Jun 1996.

[21] Yu J, Xue Y, and Song HK. Comparison of lung t2* during free-breathing at 1.5t and 3.0t with ultrashort echo time (ute) imaging. *Magn Reson Med*, 66(1):248–54, Jul 2011.

[22] Wild JM, Marshall H, Bock M, Schad LR, Jakob PM, Puderbach M, Molinari F, Van Beek EJR, and Biederer J. Mri of the lung (1/3): methods. *Insights Imaging*, 3(4):345–53, Aug 2012.

[23] Skalina S, Kundel HL, Wolf G, and Marshall B. The effect of pulmonary edema on proton nuclear magnetic resonance relaxation times. *Invest Radiol*, 19(1):7–9, Jan-Feb 1984.

[24] Nichols MB and Paschal CB. Measurement of longitudinal (t1) relaxation in the human lung at 3.0 tesla with tissue-based and regional gradient analyses. *J Magn Reson Imaging*, 27(1):224–8, Jan 2008.

[25] Stanisz GJ, Odrobina EE, Pun J, Escaravage M, Graham SJ, Bronskill MJ, and Henkelman RM. T1, t2 relaxation and magnetization transfer in tissue at 3t. *Magn Reson Med*, 54(3):507–12, Sep 2005.

[26] Florian von Knobelsdorff-Brenkenhoff, Marcel Prothmann, Matthias A Dieringer, Ralf Wassmuth, Andreas Greiser, Carsten Schwenke, Thoralf Niendorf, and Jeanette Schulz-Menger. Myocardial t1 and t2 mapping at 3t: reference values, influencing factors and implications. *J Cardiovasc Magn Reson*, 15(1):53, 2013.

[27] Bojorquez JZ, Bricq S, Acquitter C, Brunotte F, Walker PM, and Lalande A. What are normal relaxation times of tissues at 3 t? *Magn Reson Imaging*, 35:69–80, Jan 2017.

[28] Buxton RB, Edelman RR, Rosen BR, Wismer GL, and Brady TJ. Contrast in rapid mr imaging: T1- and t2-weighted imaging. *J Comput Assist Tomogr*, 11(1):7–16, Jan-Feb 1987.

[29] Hayes CE, Case TA, Ailion DC, Morris AH, Cutillo A, Blackburn CW, Durney CH, and Johnson SA. Lung water quantitation by nuclear magnetic resonance imaging. *Science*, 216(4552):1313–5, Jun 1982.

[30] Caruthers SD, Paschal CB, Pou NA, and Harris TR. Relative quantification of pulmonary edema with noncontrast-enhanced mri. *J Magn Reson Imaging*, 7(3):544–40, May-Jun 1997.

[31] Estilaei M, MacKay A, Whittall K, and Mayo J. In vitro measurements of water content and t2 relaxation times in lung using a clinical mri scanner. *J Magn Reson Imaging*, 9(5):699–703, May 1999.

[32] Holverda S, Theilmann RJ, Sá RC, Arai TJ, Hall ET, Dubowitz DJ, Prisk GK, and Hopkins SR. Measuring lung water: ex vivo validation of multi-image gradient echo mri. *J Magn Reson Imaging*, 34(1):220–4, Jul 2011.

[33] Molinari F, Madhuranthakam AJ, Lenkinski R, and Bankier AA. Ultrashort echo time mri of pulmonary water content: assessment in a sponge phantom at 1.5 and 3.0 tesla. *Diagn Interv Radiol*, 20(1):34–41, Jan-Feb 2014.

[34] Theilmann RJ, Arai TJ, Samiee A, Dubowitz DJ, Hopkins SR, Buxton RB, and Prisk GK. Quantitative mri measurement of lung density must account for the change in t(2) (*) with lung inflation. *J Magn Reson Imaging*, 30(3):527–34, Sep 2009.

[35] Lederlin M and Crémillieux Y. Three-dimensional assessment of lung tissue density using a clinical ultrashort echo time at 3 tesla: a feasibility study in healthy subjects. *J Magn Reson Imaging*, 40(4):839–47, Oct 2014.

[36] Walkup LL, Tkach JA, Higano NS, Thomen RP, Fain SB, Merhar SL, Fleck RJ, Amin RS, and Woods JC. Quantitative magnetic resonance imaging of bronchopulmonary dysplasia in the neonatal intensive care unit environment. *Am J Respir Crit Care Med*, 192(10):1215–22, Nov 2015.

[37] Hahn AD, Higano NS, Walkup LL, Thomen RP, Cao X, Merhar SL, Tkach JA, Woods JC, and Fain SB. Pulmonary mri of neonates in the intensive care unit using 3d ultrashort echo time and a small footprint mri system. *J Magn Reson Imaging*, 45(2):463–71, Feb 2017.

[38] Higano NS, Fleck RJ, Spielberg DR, Walkup LL, Hahn AD, Thomen RP, Merhar SL, Kingma PS, Tkach JA, Fain SB, and Woods JC. Quantification of neonatal lung parenchymal density via ultrashort echo time mri with comparison to ct. *J Magn Reson Imaging*, 46(4):992–1000, Oct 2017.

[39] Glover GH. Simple analytic spiral k-space algorithm. *Magn Reson Med*, 42(2):412–5, Aug 1999.

[40] Gibiino F, Sacolick L, Menini A, Landini L, and Wiesinger F. Free-breathing, zero-te mr lung imaging. *MAGMA*, 28(3):207–15, Jun 2015.

[41] Gurney PT, Hargreaves BA, and Nishimura DG. Design and analysis of a practical 3d cones trajectory. *Magn Reson Med*, 55(3):572–82, Mar 2006.

[42] Willmering MM, Robison RK, Wang H, Pipe JG, and Woods JC. Implementation of the floret ute sequence for lung imaging. *Magn Reson Med*, 82(3):1091–1100, Sep 2019.

[43] Ferreira PF, Gatehouse PD, Mohiaddin RH, and Firmin DN. Cardiovascular magnetic resonance artefacts. *J Cardiovasc Magn Reson*, 15(1):41, May 2013.

[44] Herrmann KH, Krämer M, and Reichenbach JR. Time efficient 3d radial ute sampling with fully automatic delay compensation on a clinical 3t mr scanner. *PLoS One*, 11(3), Mar 2016.

[45] Qian Y and Boada FE. Acquisition-weighted stack of spirals for fast high-resolution three-dimensional ultra-short echo time mr imaging. *Magn Reson Med*, 60(1):135–45, Jul 2008.

[46] Stobbe RW and Beaulieu C. Rapid 3d spoiled steady-state imaging with yarn-ball acquisition [abstract]. ISMRM 23rd Annual Meeting; 2015 May 30 - June 5; Toronto: Abstract nr 2442.

[47] Gai ND, Malayeri AA, and Bluemke DA. Three-dimensional t1 and t2* mapping of human lung parenchyma using interleaved saturation recovery with dual echo ultrashort echo time imaging (itsr-dute). *J Magn Reson Imaging*, 45(4):1097–1104, Apr 2017.

[48] Ehman RL, McNamara MT, Pallack M, Hricak H, and Higgins CB. Magnetic resonance imaging with respiratory gating: techniques and advantages. *AJR Am J Roentgenol*, 143(6):1175–82, Dec 1984.

[49] Oechsner M, Pracht ED, Staeb D, Arnold JF, Köstler H, Hahn D, Beer M, and Jakob PM. Lung imaging under free-breathing conditions. *Magn Reson Med*, 61(3):723–7, Mar 2009.

[50] Tibiletti M, Paul J, Bianchi A, Wundrak S, Rottbauer W, Stiller D, and Rashe V. Multistage three-dimensional ute lung imaging by image-based self-gating. *Magn Reson Med*, 75(3):1324–32, Mar 2016.

[51] Bydder M, Larkman DF, and Hajnal JV. Combination of signals from array coils using image-based estimation of coil sensitivity profiles. *Magn Reson Med*, 47(3):539–48, Mar 2002.

[52] Kellman P and McVeigh ER. Image reconstruction in snr units: a general method for snr measurment. *Magn Reson Med*, 54(6):1439–47, Dec 2005.

[53] Forbes RM, Cooper AR, and Mitchell HH. The composition of the adult human body as determined by chemical analysis. *J Biol Chem*, 203(1):359–66, Jul 1953.

[54] Ward SR and Lieber RL. Density and hydration of fresh and fixed human skeletal muscle. *J Biomech*, 38(11):2317–20, Nov 2005.

[55] Bhave G and Neilson EG. Body fluid dynamics: back to the future. *J Am Soc Nephrol*, 22(12):2166–81, Dec 2011.

[56] D'Errico JR. Understanding gridfit. https://www.mathworks.com/matlabcentral/fileexchange/8998-surface-fitting-using-gridfit, Dec 2006.

[57] Tikhonov AN. On the solution of ill-posed problems and the method of regularization. *Dokl Akad Nauk*, 151(3):501–504, 1963.

[58] Engl HW, Hanke M, and Neubauer A. *Regularization of inverse problems*. Kluwer Academic Publishers, 2000.

[59] Hansen PC. Analysis of discrete ill-posed problems by means of the l-curve. *Siam Rev*, 34(4):561–580, Dec 1992.

[60] Hansen PC and O'Leary DP. The use of the l-curve in the regularization of discrete ill-posed problems. *SIAM J Sci Comput*, 14(6):1487–1503, Nov 1993.

[61] Thompson RB, Pagano JJ, Chow K, Sekowski V, Paterson I, Ezekowitz J, Anderson T, Dyck JRB, Haykowsky MJ, and Alberta HEART investigators. Subclinical pulmonary edema is associated with reduced exercise capacity in hfpef and hfref. *J Am Coll Cardiol*, 70(14):1827–8, Oct 2017.

[62] Kauczor HU and Kreitner KF. Mri of the pulmonary parenchyma. *Eur Radiol*, 9(9):1755–64, 1999.

[63] Vinitski S, Steiner RM, Wexler HR, and Rifkin M. Assessment of lung water by magnetic resonance in three types of pulmonary edema. *Heart Vessels*, 4(2):88–93, 1988.

[64] Hatabu H, Alsop DC, Listerud J, Bonnet M, and Gefter WB. T2* and proton density measurement of normal human lung parenchyma using submillisecond echo time gradient echo magnetic resonance imaging. *Eur J Radiol*, 29(3):245–52, Mar 1999.

[65] Stock KW, Chen Q, Hatabu H, and Edelman RR. Magnetic resonance t2* measurements of the normal human lung in vivo with ultra-short echo times. *Magn Reson Imaging*, 17(7):997–1000, Aug 1999.

[66] Takahashi M, Togao O, Obara M, van Cauteren M, Ohno Y, Doi S, Kuro o M, Malloy C, Hsia CC, and Dimitrov I. Ultra-short echo time (ute) mr imaging of the lung: comparison between normal and emphysematous lungs in mutant mice. *J Magn Reson Imaging*, 32(2):326–33, Aug 2010.

[67] Ohno Y, Koyama H, Yoshikawa T, Matsumoto K, Takahashi M, Van Cauteren M, and Sugimura K. T2* measurements of 3-t mri with ultrashort tes: capabilities of pulmonary function assessment and clinical stage classification in smokers. *AJR Am J Roentgenol*, 197(2):279–85, Aug 2011.

[68] Ohno Y, Hatabu H, Murase K, Higashino T, Kawamitsu H, Watanabe H, Takenaka D, Fujii M, and Sugimura K. Quantitative assessment of regional pulmonary perfusion in the entire lung using three-dimensional ultrafast dynamic contrast-enhanced magnetic resonance imaging: Preliminary experience in 40 subjects. *J Magn Reson Imaging*, 20(3):353–65, Sep 2004.

[69] Higano NS, Hahn AD, Tkach JA, Cao X, Walkup L, Thomen RP, Merhar SL, Kingma PS, Fain SB, and Woods JC. Retrospective respiratory self-gating and removal of bulk motion in pulmonary ute mri of neonates and adults. *Magn Reson Med*, 77(3):1284–95, Mar 2017.

[70] Thompson RB, Chow K, Pagano JJ, Sekowski V, Michelakis ED, Tymchak W, Haykowsky MJ, Ezekowitz JA, Oudit GY, Dyck JRB, Kaul P, Savu A, and Paterson DI. Quantification of lung water in heart failure using cardiovascular magnetic resonance imaging. *J Cardiovasc Magn Reson*, 12(1):58, Sep 2019.

[71] Rahmer J, Börnert P, Groen J, and Bos C. Three-dimensional radial ultrashort echo-time imaging with t2 adapted sampling. *Magn Reson Med*, 55(5):1075–82, May 2006.

[72] Hopkins SR, Henderson AC, Levin DL, Yamada K, Arai T, Buxton RB, and Prisk GK. Vertical gradients in regional lung density and perfusion in the supine human lung: the slinky effect. *J Appl Physiol*, 103(1):240–8, Mar 2007.

[73] Deshmane A, Gulani V, Griswold MA, and Seiberlich N. Parallel mr imaging. *J Magn Reson Imaging*, 36(1):55–72, Jul 2012.

[74] Fujimoto S, Morikawa S, and Inubushi T. An mr comparison study of cardiogenic and noncardiogenic pulmonary edema in animal models. *J Magn Reson Imaging*, 34(5):1092–8, Nov 2011.

[75] Hedlund LW, Vock P, Effmann EL, Lischko MM, and Putman CE. Hydrostatic pulmonary edema. an analysis of lung density changes by computed tomography. *Invest Radiol*, 19(4):254–62, Jul-Aug 1984.

[76] Mansoor A, Bagci U, Xu Z, Foster B, Olivier KN, Elinoff JM, Suffredini AF, Udupa JK, and Mollura DJ. A generic approach to pathological lung segmentation. *IEEE Trans Med Imaging*, 33(12):2293–310, Dec 2014.

[77] Jaspan ON Fleysher R Lipton ML. Compressed sensing mri: a review of the clinical literature. *Br J Radiol*, 88(1056), Sep 2015.

[78] Zhu B, Liu JZ, Cauley SF, Rosen BR, and Rosen MS. Image reconstruction by domain-transform manifold learning. *Nature*, 555(7697):487–492, Mar 2018.